TECHNISCHE UNIVERSITÄT DRESDEN

Dimension-8 EFT effects in the WZ background in the ssWW EFT fit

Bachelor-Arbeit
zur Erlangung des Hochschulgrades
Bachelor of Science
im Bachelor-Studiengang Physik

vorgelegt von

Anna Franziska Reichl
geboren am 06.10.1996 in Dresden

Institut für Kern- und Teilchenphysik
Fakultät Physik
Bereich Mathematik und Naturwissenschaften
Technische Universität Dresden
2022

Eingereicht am 29. August 2022

1. Gutachter: Dr. Frank Siegert
2. Gutachter: Prof. Dr. Arno Straessner

Abstract

(English)

In search of new physics (BSM), one focus at the LHC is vector boson scattering such as the process of same charge $W^{\pm}W^{\pm}$ (ssWW) scattering. The quartic gauge couplings contributing to the process allow studies on electroweak symmetry breaking and are sensitive to possible effects of new physics. Effective field theories (EFT) are a way to quantify these BSM effects by extending the Standard Model (SM) Lagrangian by operators of higher energy dimension. The dimension-8 EFT operators are the lowest order operators only generating quartic gauge vertices, and so far, only the signal process ssWW scattering itself was considered when searching for unitarity limits of these dimension-8 operators. This thesis works with ssWW EFT samples as well as with WZ EFT samples based on Run 2 measurements of $138.7\,\mathrm{fb}^{-1}$ at ATLAS. $\pm 1\,\sigma$, $\pm 2\,\sigma$ limits for the coefficients of each operator at different clipping values of the center of mass energy of the ssWW process are extracted using either ssWW EFT samples only, or WZ EFT samples or both at once. A value of maximum validity for each operator is obtained by comparing theoretical unitarity bounds with the limits found. This procedure is done in the ssWW signal region, and for the WZ EFT samples repeated in a WZ control region.

(Deutsch)

Auf der Suche nach Physik jenseits des Standardmodells (BSM) ist ein Fokus des LHC die Streuung von Vektorbosonen (VBS), wie beispielsweise die Streuung von gleichgeladenen $W^{\pm}W^{\pm}$ (ssWW). Vierer-Vertices, die in der VBS Streuamplitude auftauchen ermöglichen Tests der elektroschwachen Symmetriebrechung und sind gleichzeitig sensitiv für mögliche BSM Effekte. Effektive Feldtheorien (EFT) sind ein Weg, solche Effekte zu quantisieren, indem der Standardmodell-Lagrangian um Terme höherer Ordnung (EFT-Operatoren und deren Kopplungskonstanten) erweitert wird. Die dimension-8 EFT-Operatoren sind die Operatoren niedrigster Ordnung, die nur Vierer-Vertices generieren. Bisher wurde nur der Signalprozess ssWW-Streuung betrachtet, wenn nach Unitaritätslimits für solche Operatoren gesucht wurde. Diese Arbeit verwendet ssWW EFT samples und WZ EFT samples, die auf Run 2 Messungen von $138.7\,\mathrm{fb}^{-1}$ am ATLAS-Experiment basieren. Für die Kopplungskoeffizienten jedes Operators werden $\pm 1\,\sigma$, $\pm 2\,\sigma$ Limits bei verschiedenen clipping-Werten der Schwerpunktsenergie des ssWW Prozesses extrahiert, dabei werden entweder nur ssWW EFT samples, nur WZ EFT samples oder beide gleichzeitig verwendet. Für jeden Operator wird jeweils in der ssWW Signalregion und für die WZ EFT samples auch in einer WZ control region ein Wert maximaler Gültigkeit in Bezug auf Unitarität ermittelt.

Contents

1 Experimental framework

1.1 LHC

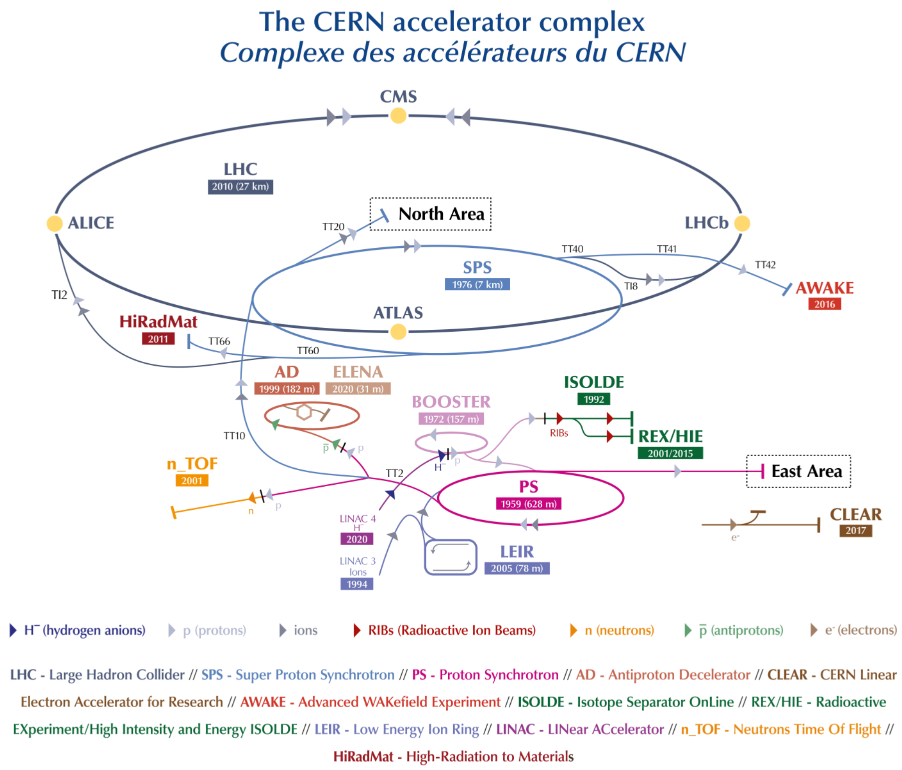

Figure 1.1: The CERN accelerator complex in 2019. Naming follows the pattern "unit, year when first switched on (circumference)".[1]

The Large Hadron Collider (LHC) is the worlds largest particle accelerator situated near Geneva, built from 1998 until 2008 by CERN (European Organization for Nuclear Research). Its purpose is the search for new physics, its design is optimized to deliver very high collision energies and luminosities. General structure of the LHC and its relation to the other accelerator units is depicted in Figure 1.1. The LHC itself is the last unit in a chain of consecutive accelerators, which accelerate beams of particles and forward them to the next unit. Along its circumference of 27 km, the LHC hosts four main experiments: Alice (A Large Ion Collider Experiment), ATLAS (A Toroidal LHC ApparatuS), CMS (Compact Muon Solenoid), LHC-b (Large Hadron Collider beauty). Inside the LHC, two beams travel in opposite directions in separate beam pipes in ultrahigh vacuum. Those beams reached energies of 6.5 TeV during Run 2, only intersecting at the experiments, with a centre-of-mass energy (total collision energy) of $\sqrt{s} = 13\,\mathrm{TeV}$.

For a given $\sqrt{s}$ the rate of events per second $\frac{dN}{dt}$ is calculated as

$$\frac{dN}{dt} = L\sigma \tag{1.1}$$

with the cross section σ (which includes process specific properties) and the luminosity L, summarizing setup specific dependencies:

$$L = \frac{N_b^2 n_b f}{4\pi\sigma_x\sigma_y} F \tag{1.2}$$

where n_b is the number of bunches per beam, N_b is the number of particles per bunch, f is the revolution frequency and σ_i is the beam width for Gaussian beam profiles. F is a beam shape correction factor. During Run 2 luminosities of $150\,\mathrm{fb}^{-1}$ where recorded.[2, 3, 4]

1.2 ATLAS

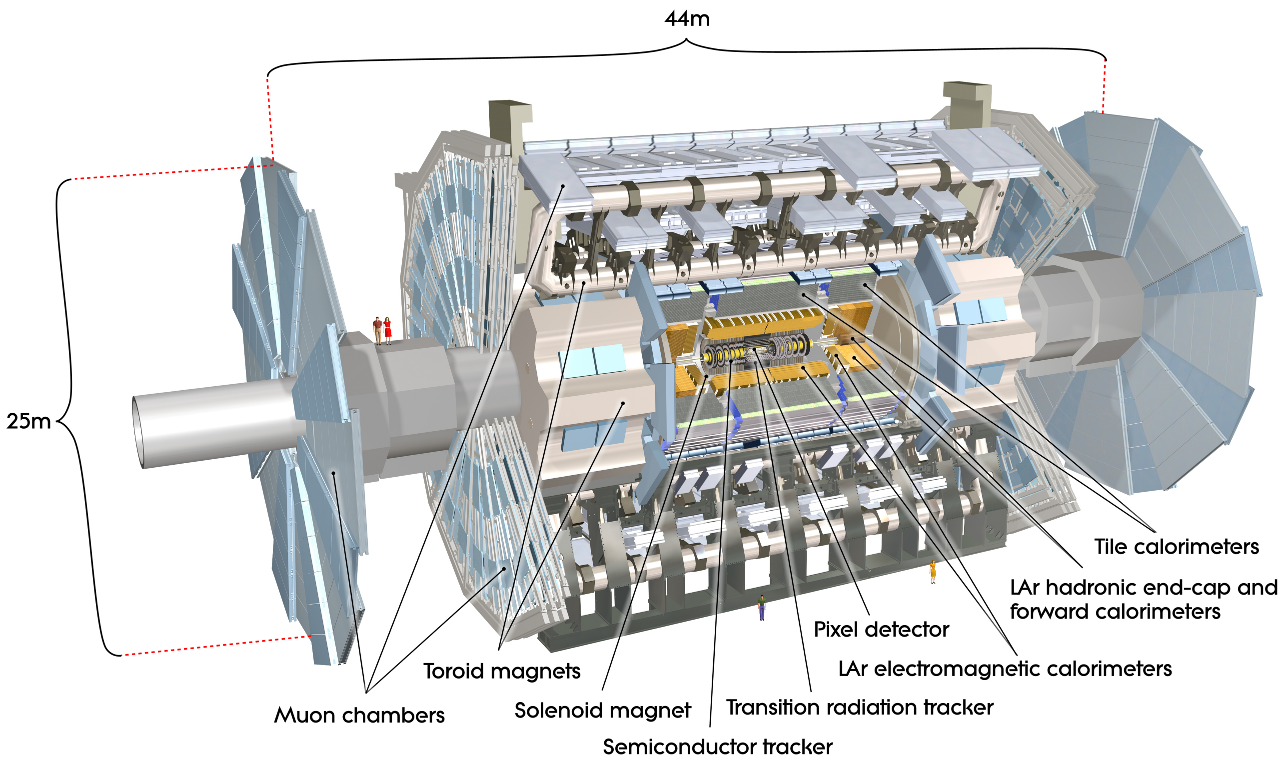

Figure 1.2: Schematic sketch of the ATLAS detector.[5]

This thesis works with data based on Run 2 measurements of $138.7\,\mathrm{fb}^{-1}$ of the ATLAS detector. Figure 1.2 shows the concentric symmetric construction around the beam pipe. High precision measurement of particle energies and momenta as well as their charge is enabled by the different layers of the setup: the inner detector system, responsible for track reconstruction; electromagnetic and hadronic calorimeters, catching most SM particles except for muons and neutrinos, of which the latter cannot be detected by ATLAS; the muon spectrometer which is able to detect and measure muons.

The particle identification is based on different principles in each layer.

The inner detector is able to trace charged particles with the help of a system of magnets parallel to the beam axis. Different curvatures in the transverse plane allow the reconstruction of the transverse momenta and the charge of the particles.

In the calorimeters, all electromagnetically or hadronically interacting particles store their complete energy in the according layer, which allows the detection of neutral photons and hadrons. Calorimeters are used to find the missing transverse energy of an event or the energy of jets.

Since muons are 200 times heavier than electrons they pass through the inner detector and subsequent layers without losing a lot of energy. The muon spectrometer is able to conclude on the momenta and charge of muons by track reconstruction.[4]

2 Theoretical framework and utilized methods

2.1 Effective field theories

The Standard Model of particle physics (SM) has some shortcomings that require further research: for example it excludes Gravity, there is evidence for Dark Matter of unknown composition, and the SM disagrees with experimental findings on the mass of neutrinos. In general, the search for answers to these unresolved issues is referred to as Beyond Standard Model physics (BSM). This new physics might be found in two ways: directly, as happened when the Higgs boson was discovered - its mass was directly measured as the result of decay product reconstruction after a proton-proton collision; or it may be found indirectly. The indirect approach means that we only observe residual effects of the new physics, e.g. as a deviation from the SM prediction in the tail of a kinematic distribution of a certain variable.
Effective Field Theories (EFTs) are a tool to quantify these variations from SM, effective meaning that they are not complete theories but only describe physics in a certain range of validity.[6, 7] They belong to an underlying complete theory that is (yet) unknown, and the idea of the EFTs is to describe not just one specific BSM phenomenon but to be open for new physics to come from a broad spectrum causes. At the same time, if there is no new physics discovered in the validity range covered by the EFT it also provides an accuracy with which BSM effects are excluded.[2] The effective Lagrangian $\mathcal{L}_{\text{eff}}$ for an EFT is essentially the SM Lagrangian $\mathcal{L}_{\text{SM}}$, expanded by terms of higher energy dimensions, namely terms for EFT operators of higher dimension:

$$\mathcal{L}_{\text{eff}} = \mathcal{L}_{\text{SM}} + \sum_i \frac{c_i^{(6)}}{\Lambda^2}\mathcal{O}_i + \sum_j \frac{c_i^{(8)}}{\Lambda^4}\mathcal{O}_j + ... \tag{2.1}$$

Here, $\mathcal{O}_{i,j}$ are dimension-6,8 operators, the Wilson coefficients c_i parametrize the coupling strength to the SM, Λ is the scale of the new physics. In this analysis, as is common practice, the simplified parameters $f_j = \frac{c_i^{(8)}}{\Lambda^4}$ will be used for the investigated dimension-8 operators. Note that the validity of an EFT is given only for energies $E < \Lambda$, so below the energy scale of the new physics.[8]

2.2 Same-sign $W^\pm W^\pm jj$

Same-sign $W^\pm W^\pm$ (ssWW) scattering is a form of vector boson scattering (VBS), that is not observable as an isolated process in detector experiments. It occurs as a sub-process of $W^\pm W^\pm jj$, the production of two W bosons of same charge (same-sign) and two jets resulting from a proton-proton collision:

$$pp \rightarrow W^{\pm}W^{\pm} + 2\text{jets} \rightarrow l^{\pm}\nu l^{\pm}\nu + 2\text{jets} \tag{2.2}$$

The schematic structure of this process can be seen in Figure 2.3. A proton consist of two up and one down quark. From the initial state protons one quark each emits a $W^{\pm}$ boson. The two final state quarks have high absolute values of rapidity and large momenta. The two typical jets are the result of hadronization of the final state quarks. Those so-called tagging jets live in opposite hemispheres and have a notable difference in rapidity (Δy_{jj}) and high invariant mass (m_{jj}). The two same-sign leptons normally are found between the tagging jets Figure 2.1.[8, 3]
All this knowledge about these properties of the process is utilized to build the ssWW signal region. This essentially means designing a set of selection criteria that pick mostly events from the desired process and leave you with a small and well-defined background. Some details are listed in Table 2.1, detailed information may be found in.[8]
The underlying process for which all this sorting out took place - ssWW - has five possible leading order Feynman diagrams (Figure 2.2) contributing to its scattering amplitude, in Figure 2.3 they are represented by the placeholder-circle. Same-sign $W^{\pm}W^{\pm}$ is dominated by elektroweak production, allowing the testing of the electroweak symmetry breaking predictions from the SM. In addition the quartic gauge couplings that make up the amplitude of the process are sensitive to possible BSM effects.[8] This sensitivity is parametrized using the EFTs introduced earlier.

The first operators in Equation 2.1 that lead to quartic gauge coupling without any association to triple gauge coupling are those of dim8 (at dim6 quartic vertices are also generated, but never without triple gauge boson vertices).[9] Only the 8 operators of dimension-8 that affect ssWW processes will be described here (there are more that affect other processes, they are listed in

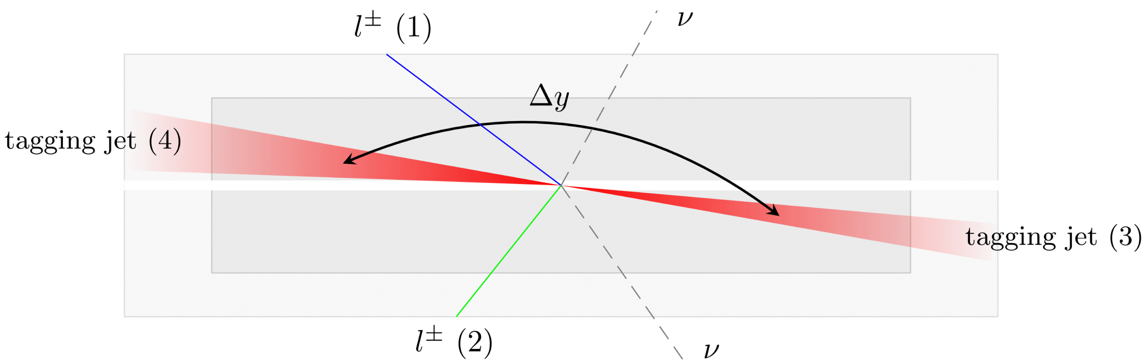

Figure 2.1: Topology of the ss$W^{\pm}W^{\pm}jj$: 2 tagging jets (3, 4) with same-sign leptons (1, 2) (plus the undetectable neutrinos) between them.[4]

Table 2.1: Event selection for the ssWW signal region adopted from [8].

Exactly two signal leptons with $p_T > 27\,\mathrm{GeV}$ and the same electrical charge with $\lvert\eta\rvert < 2.5$ for muons and with $\lvert\eta\rvert < 2.47$ excluding $1.37 \leq \lvert\eta\rvert \leq 1.52$ for electrons with $\lvert\eta\rvert < 1.37$ in the ee channel
$m_{ll'} \geq 20\,\mathrm{GeV}$
remove events with three or more preselected leptons
$\lvert m_{ee} - m_Z\rvert > 15\,\mathrm{GeV}$ in the ee-channel
$E_T^{miss} \geq 30\,\mathrm{GeV}$
at least two jets leading jet: $p_T > 65\,\mathrm{GeV}$, subleading jet: $p_T > 35\,\mathrm{GeV}$
$m_{jj} \geq 500\,\mathrm{GeV}$
b-jet veto using the DL1r tagger with the 85 % efficiency working point
$\lvert\Delta y_{jj}\rvert > 2$

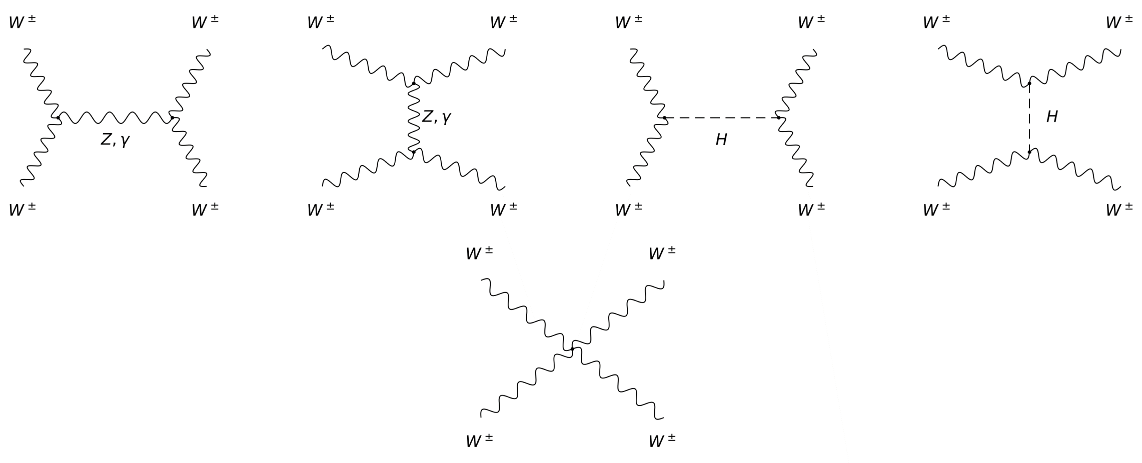

Figure 2.2: Leading order Feynman diagrams connecting two initial $W^{\pm}$ with two final $W^{\pm}$.[2]

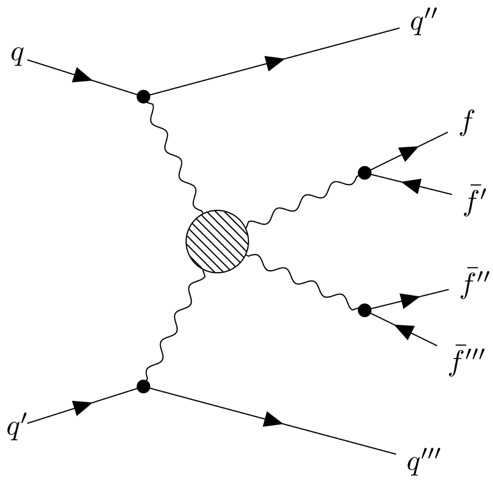

Figure 2.3: Schematic structure of electroweak gauge boson scattering.[3]

[10, 9]). These operators are all CP conserving, and belong to three different classes, each built from Φ, the Higgs doublet, the covariant derivative $D_\mu\Phi = (\partial_\mu + igW_\mu^j\frac{\sigma^j}{2} + ig'B_\mu\frac{1}{2})\Phi$ with the Pauli matrices $\sigma^j (j = 1,2,3)$ and/or the $SU(2)_\mathrm{L}$ field strength $\hat{W}_{\mu\nu} \equiv W_{\mu\nu}^j\frac{\sigma^j}{2}$.
The operators will be called by their indices here, such that for example S0 represents $\mathcal{O}_{S,0}$.
S0 and S1 contain covariant derivatives of the Higgs field only:

$$\begin{aligned}
\mathcal{O}_{S,0} &= [(D_\mu\Phi)^\dagger D_\nu\Phi] \times [(D^\mu\Phi)^\dagger D^\nu\Phi] \\
\mathcal{O}_{S,1} &= [(D_\mu\Phi)^\dagger D^\mu\Phi] \times [(D_\nu\Phi)^\dagger D^\nu\Phi]
\end{aligned} \tag{2.3}$$

The operators M0, M1 and M7 contain 2 covariant derivatives and two field strengths:

$$\begin{aligned}
\mathcal{O}_{M,0} &= \mathrm{Tr}[\hat{W}_{\mu\nu}\hat{W}^{\mu\nu}] \times [(D_\beta\Phi)^\dagger D^\beta\Phi] \\
\mathcal{O}_{M,1} &= \mathrm{Tr}[\hat{W}_{\mu\nu}\hat{W}^{\nu\beta}] \times [(D_\beta\Phi)^\dagger D^\mu\Phi] \\
\mathcal{O}_{M,7} &= [(D_\mu\Phi)^\dagger\hat{W}_{\beta\nu}\hat{W}^{\beta\mu}D^\nu\Phi]
\end{aligned} \tag{2.4}$$

And the operators T0, T1, T2 contain field strengths only:

$$\begin{aligned}
\mathcal{O}_{T,0} &= \mathrm{Tr}[\hat{W}_{\mu\nu}\hat{W}^{\mu\nu}] \times \mathrm{Tr}[\hat{W}_{\alpha\beta}\hat{W}^{\alpha\beta}] \\
\mathcal{O}_{T,1} &= \mathrm{Tr}[\hat{W}_{\alpha\nu}\hat{W}^{\mu\beta}] \times \mathrm{Tr}[\hat{W}_{\mu\beta}\hat{W}^{\alpha\nu}] \\
\mathcal{O}_{T,2} &= \mathrm{Tr}[\hat{W}_{\alpha\mu}\hat{W}^{\mu\beta}] \times \mathrm{Tr}[\hat{W}_{\beta\nu}\hat{W}^{\nu\alpha}]
\end{aligned} \tag{2.5}$$

2.3 Maximum likelihood

The maximum likelihood method is a procedure for estimating the parameters of a given probability distribution. This is very helpful when only n uncorrelated measurements x_i are known - those will be the random variables of the probability density $f(x|a)$, where a is the parameter characterizing f. The product $f(x_i|a)[x_i, x_i+dx_i]$ is the probability of finding the measurement x_i within the interval $[x_i, x_i + dx_i]$; multiplying all those probabilities for all n measurements would give the full probability for the complete measurement, but since the intervals $[x_i, x_i+dx_i]$ do not depend on the parameter a they are omitted and an optimization is instead performed for the simplified likelihood function:

$$\mathcal{L}(a) = \prod_{i=1}^{n} f(x_i|a) \qquad\qquad \frac{\partial \mathcal{L}}{\partial a}\bigg|_{a=\overline{a}} = 0 \tag{2.6}$$

The value $\overline{a}$, which maximizes the likelihood function for the given set of measurements will be called best fit value for the parameter a. It is common to use the negative logarithmic likelihood function $\mathcal{F}$ and determine its minimum to find $\overline{a}$:

$$\mathcal{F} = -2\ln\mathcal{L} = -2\sum_{i=1}^{n} \ln(f(x_i|a)) \tag{2.7}$$

This is practical because if for $n \to \infty$ $\mathcal{L}$ behaves like a Gaussian, it is very easy to determine the $\pm 1\,\sigma$, $\pm 2\,\sigma$ ranges (i.e. the 68 % and 95 % confidence level limits). They are to be found at $\mathcal{F}(a) - \mathcal{F}(\overline{a})$ equals one and four respectively. To account for asymmetries that might occur, we will always compute the negative and positive $\pm 1\,\sigma$, $\pm 2\,\sigma$ values separately.[11]

In the following analysis maximum likelihood scans will be used to find those $\pm 1\,\sigma$, $\pm 2\,\sigma$ limits for the simplified coefficients in the effective Lagrangian, which will be performed using the EFTfun framework.[12] For this thesis a blind analysis is performed: the real data stay blinded and instead, the fits are performed on one single representative pseudo data set, which sums over background and signal leading order distributions. This representative data set is sometimes referred to as asimov data set[1].[14] Only scans for the coefficient of one operator at the time are performed, setting all remaining coefficients to zero.

2.4 Monte Carlo simulation

Data simulations offer a way to refine and optimize analysis tools, test predictions from theories or estimate what backgrounds are to be expected within real data. In the case of EFTs

[1] Asimov was a science fiction author who is well known for (publicly) groping woman.[13]

introduced earlier, the theory first delivers a framework to quantify possible deviations from SM predictions. The task is to estimate the unitarity limits of this theory using MC generated datasets. When the theoretical framework is set and the real data would contain deviations from the SM, the analysis would be sensitive enough to know if they came from BSM physics belonging to the EFT.

Put very briefly, Monte Carlo generators work as follows:

The LHC does accelerate hadrons, namely protons, but the actual collision takes place at a much smaller scale, at the level of the protons building blocks, called partons (quarks and gluons). The initial state of the hadrons is well known but the event generator needs to randomly pick the initial state partons from parton distribution functions. The fist step in simulating is the hard process, which is the scattering process at parton level. Here, perturbation theory is employed to calculate matrix elements, and the Monte Carlo method is involved in the cross section calculation. The next step is the QCD parton shower, its purpose is to simulate further parton radiation associated with the gauge structure of QCD. Any parton occuring in the initial or final state is colored and able to emit gluons which in turn give rise to the formation of quark-antiquark pairs - this is referred to as parton shower. The transfer from partons back to colorless observable hadrons is called hadronization.

Due to the lack of theoretical description for problems like color confinement, processes involving QCD require modelling, essentially sets of assumptions. One such consideration is the question on how to ensure conservation of momentum when gluons are emitted by partons that are part of one of the jets in Figure 2.1. One possibility would be to distribute the recoil from that parton emission over a large group of colored particles (global recoil strategy). The samples utilized in this thesis use a dipole recoil scheme, where the recoil stays within the jet that produced the parton in question, the jets are QCD-separated.[4, 15]

The results from the hard scattering process with all its sub processes is called truth level. Thereafter, the interactions of the resulting particles with the detector are simulated, which is called detector or reconstruction level.[16]

This thesis uses EFT samples generated with MadGraph5_aMC@NLO described in detail in [17].

2.5 Decomposition and clipping techniques

Since the EFT operators are simply added to the SM Lagrangian, the matrix element of a subprocess can be written as

$$\left| A_{SM} + \sum_i \frac{c_i}{\Lambda^4} A_i \right| \tag{2.8}$$

where A_{SM} is the SM amplitude corresponding to the SM cross section and A_i are the contributions of the individual dimension-8 operators with the Wilson coefficients c_i. The matrix element (total amplitude) squared at the EFT point i is then given by

$$\left| A_{SM} + \sum_i \frac{c_i}{\Lambda^4} A_i \right|^2 = |A_{SM}|^2 + \underbrace{\sum_i \frac{c_i}{\Lambda^4} 2\,\mathrm{Re}(A_{SM} A_i)}_{\text{interference term}} + \underbrace{\sum_i \frac{c_i^2}{\Lambda^8} |A_i|^2}_{\text{quadratic term}} + \underbrace{\sum_{ij, i \neq j} \frac{c_i c_j}{\Lambda^8} 2\,\mathrm{Re}(A_i A_j)}_{\text{cross terms}} \tag{2.9}$$

Where the first term is the SM amplitude, the second term (interference term) is the amplitude of the interference between EFT operators and SM, the third term (quadratic term) represents pure EFT operator contributions and the last term (cross term) describes the interference between two operators. As stated in [8] MadGraph allows to generate samples using only one of those terms at a time (amplitude decomposition), this is the reason why it is possible to compare the individual yields for each of them (the cross terms are ignored in this thesis). The divergence of the quartic gauge-boson interactions from SM will lead to a growth in scattering amplitudes, indicating the existence of new physics.[10]

Any nonzero anomalous quartic gauge-boson couplings will violate unitarity at sufficiently high energies. As suggested in [18] and applied already in [2, 19], this thesis will use clipping in order to find cut-off energies E_{cut} where the EFTs violate unitarity. From this E_{cut} upwards, the EFT predictions will be set to zero while keeping SM predictions even beyond that energy.

The first part of the analysis utilized CAF, the Common Analysis Framework.[20] With its help histograms at different cutflow levels where created: like the selection criteria for the SR, it is possible to implement a criterion that limits the truth level variable $m_{ll\nu\nu}^{truth}$ to a certain value. This is done for multiple clippings at 1, 1.5, 2 and 5 TeV as well as without any such limitation, which will be referred to as clipping value ∞. The $\pm 1\,\sigma$, $\pm 2\,\sigma$ values for the coefficient of each operator will be plotted against those clippings, and compared to the unitarity limits belonging to the scenario where just one coefficient is not vanishing (those are listed in Table 8.1). The impact of removing events is evaluated on the m_{ll} distribution .

It is desirable to increase the range of validity for each of the operators to gain a theory that describes possible SM deviations within an energy range as large as possible. This would be achieved by reducing the $\pm 2\,\sigma$ ranges, such that they stay inside the unitarity bounds for as long as possible.

3 Sample Validation

Following a previous study [2] this thesis will be working with the reconstruction level variable m_{ll} as it proved sensitive and useful for BSM research (dilepton invariant mass: $m_{ll} = \sqrt{|\vec{p}_{l_1}||\vec{p}_{l_2}|(1 - \cos(\Delta\theta(l_1 l_2)))}$ with $\vec{p}_l$ being the momentum of the lepton and their scattering angle $\cos(\Delta\theta(l_1 l_2))$). All the histograms show kinematic distributions of the variable m_{ll} unless otherwise specified. In order to produce comparable results this variable will be used in the ssWW signal region as well as the WZ control region. The analysis in [2] already did a binning optimization, for simplicity that binning will be adopted for both the ssWW signal region (same as in [2]) and the additional WZ control region (CR): $[0, 100, 200, 300, 410, 590, 1000]$.

This thesis uses an updated version of the EFT samples from [2], and additional WZ EFT samples. The difference between the old and the new ssWW EFT samples is the usage of a dipole recoil scheme, which eliminates some unwanted radiation in the central region of rapidity of the process.[8] The variable m_{ll} is expected to not be affected significantly by this change: since the VBS is a colorless process it would not take part in the momentum preservation task even with a global recoil scheme, jet related variables like the rapidity gap Δy_{jj} between the tagging jets are more likely to be affected. Additionally the lepton selection was aligned with the publication [8]. To verify that the new samples conform with already established ones a rough validation is performed: Table 3.1 compares the yields from the new EFT samples with those found in the support note [8] and the ones from the nominal sample (sample used as a reference point in [8]). Figure 3.1 shows the kinematic distribution of the variable m_{ll} as predicted by the nominal sample and by the new EFT sample for the for the electroweak processes ssWW and WZ. Both plots show a normalization difference between the samples. This may arise from the different shower algorithms used in the MC simulation: for the nominal sample Herwig7 is employed and the EFT samples Pythia8. In the bottom panel for ssWW a trend for a shape difference is visible, the difference between the samples rising to approximately 20 %. More information on the samples used may be found in the support note [8].

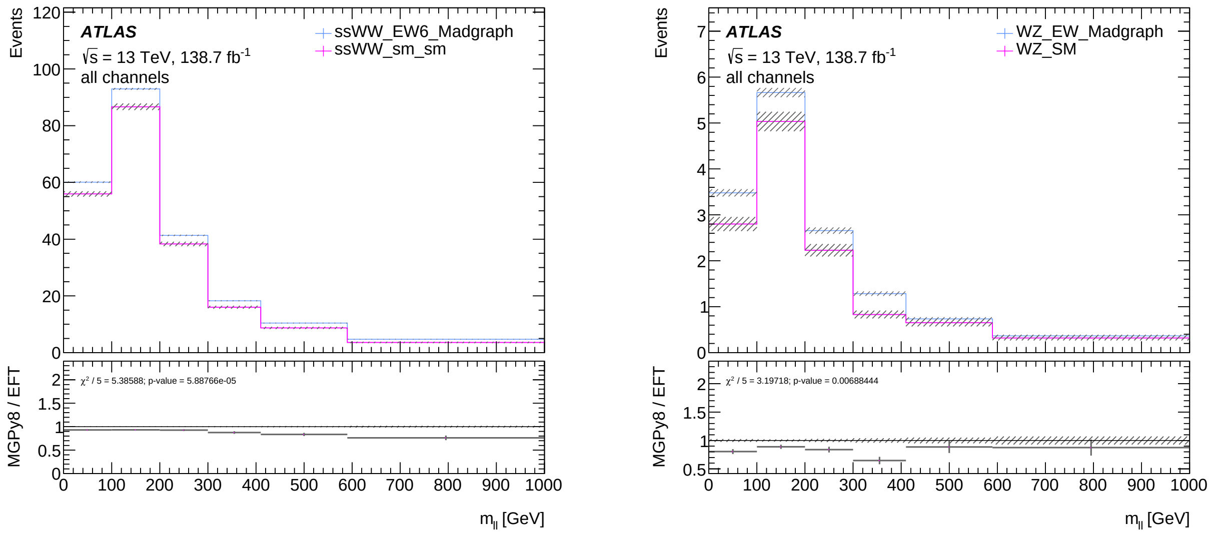

(a) ssWW **(b)** WZ

Figure 3.1: Dilepton invariant mass distribution, comparing the a) ssWW and b) WZ EWK6 nominal samples with the new ssWW EFT sample and the WZ EFT sample respectively; the subplots show the ratio between the two distributions compared; the binning was adopted from [2]; these histograms live in the SR, no clipping applied.

Table 3.1: Yield comparison between EFT sample and the support note ([8]); the ssWW_EW6_Madgraph and the WZ_EW_Madgraph (WZ_QCD) are the yields from the nominal sample, the ssWW_sm_sm and WZ_SM are those from the EFT samples, each directly beneath their nominal counterpart; the left column includes statistical uncertainties on MC estimations, the right column shows statistical, theory, and experimental systematic uncertainties.

	all	VBS support note
ssWW_EW6_Madgraph	227.793 ± 0.528	234.900 ± 0.000 ± 5.953 ± 3.831
ssWW_sm_sm	209.211 ± 1.777	
ssWW_QCD	23.651 ± 0.141	24.042 ± 0.157 ± 7.005 ± 0.635
ssWW_Int	7.366 ± 0.074	7.594 ± 0.077 ± 0.440 ± 0.116
WZ_QCD	100.925 ± 1.222	} 100.746 ± 1.177 ± 2.387 ± 6.262
WZ_EW_Madgraph	14.187 ± 0.159	
WZ_SM	11.865 ± 0.318	
Vgamma	20.145 ± 7.922	25.200 ± 3.248 ± 0.000 ± 10.117
OtherPrompt	4.092 ± 0.186	3.690 ± 0.172 ± 0.000 ± 1.052
ChargeFlip	4.995 ± 1.309	10.093 ± 0.310 ± 0.000 ± 3.675
NonPrompt	26.348 ± 3.621	55.838 ± 5.408 ± 0.000 ± 9.900

4 ssWW signal region

Based on the characteristics of the ssWW VBS process described earlier the ssWW signal region (SR) was built to select as many ssWW events as possible while simultaneously reducing backgrounds from other SM processes. Further details on the selection criteria can be found in Table 2.1 and [8].
The following section will first look at the ssWW signal region (SR) and extract limits for the EFT operators regarding only the ssWW process, these results are briefly compared to the ones [2] found. The next step is to extract limits for the same operators considering WZ EFT samples only, and finally to examine these limits for ssWW and WZ combined in the SR.

4.1 EFT limits for ssWW EFT in ssWW SR

The EFTfun tool [12] outputs plots of the logarithmic maximum likelihood function for each operator at each clipping value and prints out five values for each plot: $\pm 1\,\sigma$, $\pm 2\,\sigma$ and the best fit value. For the scans investigating the ssWW samples, those plots all have a parabolic shape with minima close to zero like the one depicted in Figure 4.2. The location of the minimum arises from the fact that the pseudo data sets where used for the fit. The slopes vary from scan to scan. The limits for the coefficients of the dimension-8 operators M0, M1, M7, S0, S1, T0, T1, T2 are shown in Table 8.10 to Table 8.15. Those results are transferred into clipping scans like the one for M7 in Figure 4.1. The clipping scans for the other operators are to be found in the Appendix. For most of the operators the behavior of the clipping scans looks similar: the $\pm 2\,\sigma$, $\pm 1\,\sigma$ decrease steadily from clipping energy $E_c = 1\,\mathrm{TeV}$ down to the limits at clipping ∞. For the operators T1 and T2 the positive 1 and $2\,\sigma$ limits rise between the clippings $1\,\mathrm{TeV}$ and $1.5\,\mathrm{TeV}$. Looking at Table 8.7 in the Appendix, the last three columns show the ratio between the contributions of interference (int) and quadratic (quad) terms adding to the scattering amplitude for the operator in question (T2) for each scenario: when scanning only ssWW EFT parts, WZ alone and both combined (called combi). For $E_c = 1.5\,\mathrm{TeV}$ this ratio int/quad is dominated by the interference term which is not the case for the previous and the following clippings. For the operator T1 the ratio increases because of the growth difference between interference and quadratic term. In the next section it will be illustrated that this gives rise to a more asymmetric shape of the logarithmic maximum likelihood scans and therefore may change the slope of the clipping scans. The maximum validity for each operator can be easily extracted from the clipping plots as the minimum intersection of the $\pm 2\,\sigma$ lines with the according unitarity bound from Table 8.1 in the Appendix. The results can be found in Table 4.1: except for the operator S1 the limits improve (grow) compared to those found in [2].

Table 4.1: Comparison between maximum validity for each operator from previous work [2] with those found in this thesis.

	maximum validity, m_{ll} [TeV]			
	ssWW previous	ssWW in SR	combi in SR	WZ in CR
M0	1.26	1.33	1.34	1.86
M1	1.69	1.77	1.77	1.69
M7	1.86	2.0	-	-
S0	1.60	1.61	-	-
S1	-	-	-	-
T0	1.55	1.64	1.59	1.58
T1	2.35	2.37	2.43	1.98
T2	1.78	1.88	1.89	1.76

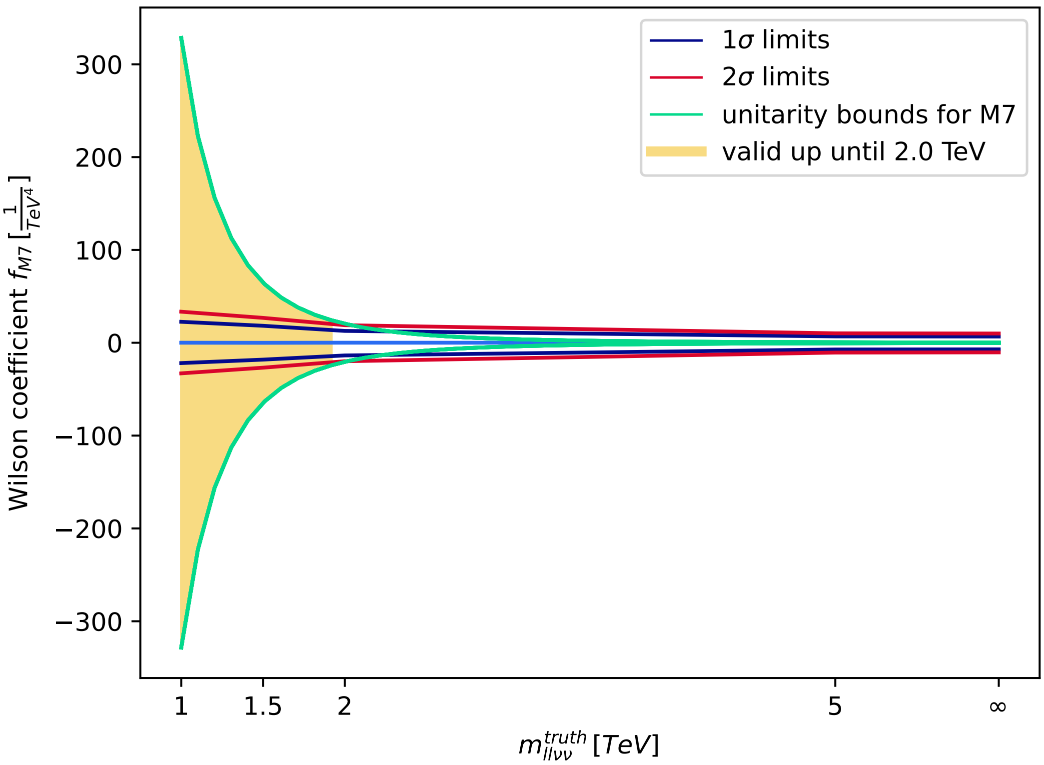

Figure 4.1: Clipping scan for ssWW in SR for the operator M7.

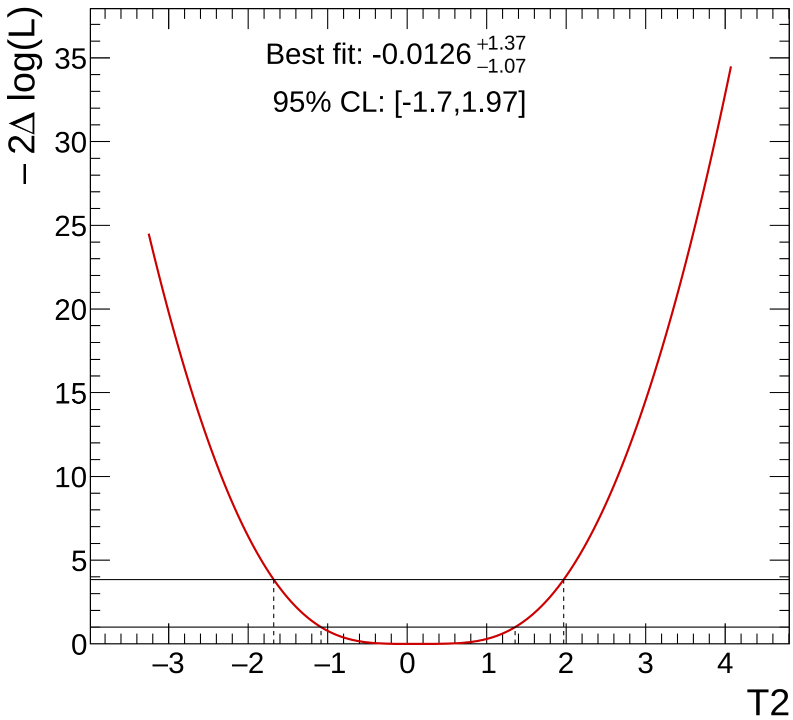

Figure 4.2: Negative logarithmic maximum likelihood scan for the operator T2, using ssWW EFT samples in the SR at clipping value 1 TeV (output from EFTfun tool).

4.2 EFT limits for WZ in ssWW SR

For WZ the EFT samples provided only included the WZ EFT interference sample for S0, the quadratic one was missing, and for M7 there where no WZ EFT samples. Hence, no further examination of these operators was performed.

Extracting the limits for WZ EFT shall serve as a comparison point: better limits are expacted in the WZ control region employed later on, and WZ fits in the SR will help understand the scans combining both ssWW and WZ EFTs in the SR.

In the Figures 8.2a, 8.4a, 8.7a, 8.9a, 8.11a, 8.13a the clipping scans for the WZ samples in the SR are depicted. Because of several obstacles it was decided to not extract the maximum validity values for WZ in the SR. The maximum likelihood scans for the operators T0 and S1 showed double minima. For S1 the evolution of the double minimum from one clipping to the next (shown in Figure 4.3a, Figure 4.3b) gives rise to a huge jump in the $2\,\sigma$ line in the clipping plot Figure 8.7a. The reason for the asymmetric behavior lies in the interference term: when only taking the quadratic term into account, the double minimum as well as any asymmetry vanish. This can be seen in Figure 4.3c.

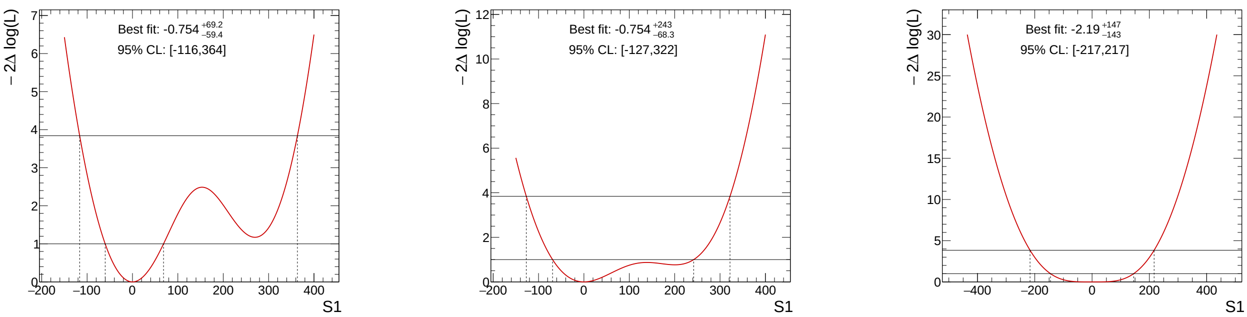

(a) $E_c = 1\,\mathrm{TeV}$ **(b)** $E_c = 1.5\,\mathrm{TeV}$ **(c)** $E_c = 1\,\mathrm{TeV}$, quad only

Figure 4.3: Negative logarithmic maximum likelihood scans for S1 in the SR using WZ EFT samples only. The evolution of the double minimum between the clippings at 1 and $E_c = 1.5\,\mathrm{TeV}$ shifts the $1\,\sigma$ intersection to a much higher value. The rightmost plot shows the scan when omitting the interference term, demonstrating that the asymmetries arise form the interference contribution.

For T0 it was not possible to convince the EFTfun tool to output the upper $2\,\sigma$ value at the end of the second minimum (scans depicted in Figure 4.4). This problem reflects in the clipping scan Figure 8.9a: it is not possible to find the actual validity range here since the $2\,\sigma$ value for $E_c = 1\,\mathrm{TeV}$ is distorted.

For M1 Table 8.3 shows an decrease of the yields for the WZ interference term between the clipping value 1 TeV and 1.5 TeV. The reason for this behaviour can be found in the histograms in Figure 4.5: when clipping at 1 TeV, the interference term for WZ becomes less negative in

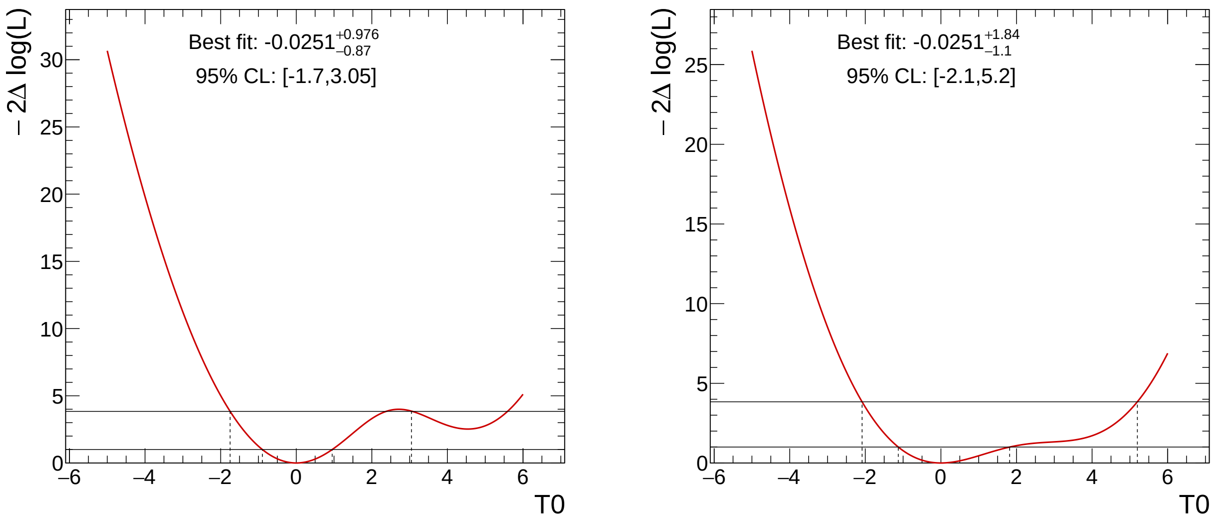

(a) $E_c = 1\,\mathrm{TeV}$ (b) $E_c = 1.5\,\mathrm{TeV}$

Figure 4.4: Negative log likelihood scan for WZ for operator T0 in the SR, showing two minima. For $E_c = 1$ TeV the software recognizes only one intersection of the curve with the $2\,\sigma$ line in the positive x-range at a time, finding the two left ones depending on the scanning range, but never the one rightmost (output from EFTfun tool).

the last bin compared to clipping at 1.5 TeV. Since the yields sum over all the WZ interference entries, they will decrease from one clipping to the next. The histograms in Figure 4.6 from [21] illustrate quite nicely the principle behind the different behaviours of the quadratic and the interference term: they depict the distribution on which the clippings are applied. Depending on the clipping, the ratio between quadratic and interference contribution varies, and the interference ones are more or less negative. A similar picture would arise when plotting this truth level variable for the samples used in this thesis.

4.3 EFT limits for comibined ssWW and WZ in ssWW SR

Figure 4.7 shows fits for the coefficient for T0 in the signal region again, now considering both ssWW and WZ EFTs. The result still shows a slight asymmetry (which may be more evident to the eye in the clipping scans in Figure 8.8b or simply in **??**) but there are no double minima confusing the EFTfun tool anymore.

In Table 4.2 we can see an overview on the EFT limits on the coefficients for each operator when no clipping is applied: the improvement (i.e. decrease in absolute value) for ssWW in the SR from the previous fits [2] to the fits performed in this thesis are clearly bigger than the gain from ssWW alone to the combined fit. The the former ranges from 7.25 % up to 16.76 %, whereas the latter ranges from −4.55 % to 6.98 %. The negative improvement, i.e. worsening

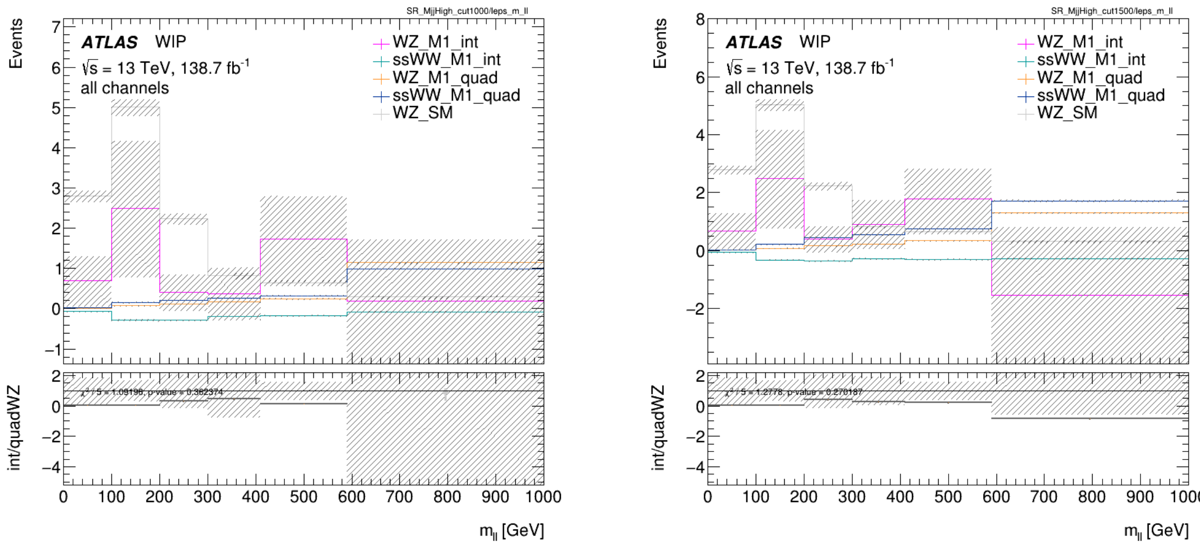

(a) $E_c = 1\,\text{TeV}$

(b) $E_c = 1.5\,\text{TeV}$

Figure 4.5: Kinematic distribution of m_{ll} for M1 in SR showing the WZ SM prediction and the interference and quadratic terms of ssWW EFT predictions and the WZ EFT predictions. For display purposes the operator M1 has an coefficient $\frac{c_n}{\Lambda^4} = 10\,\text{TeV}^{-1}$ for the ssWW sample and $\frac{c_n}{\Lambda^4} = 28\,\text{TeV}^{-1}$ for the WZ sample.

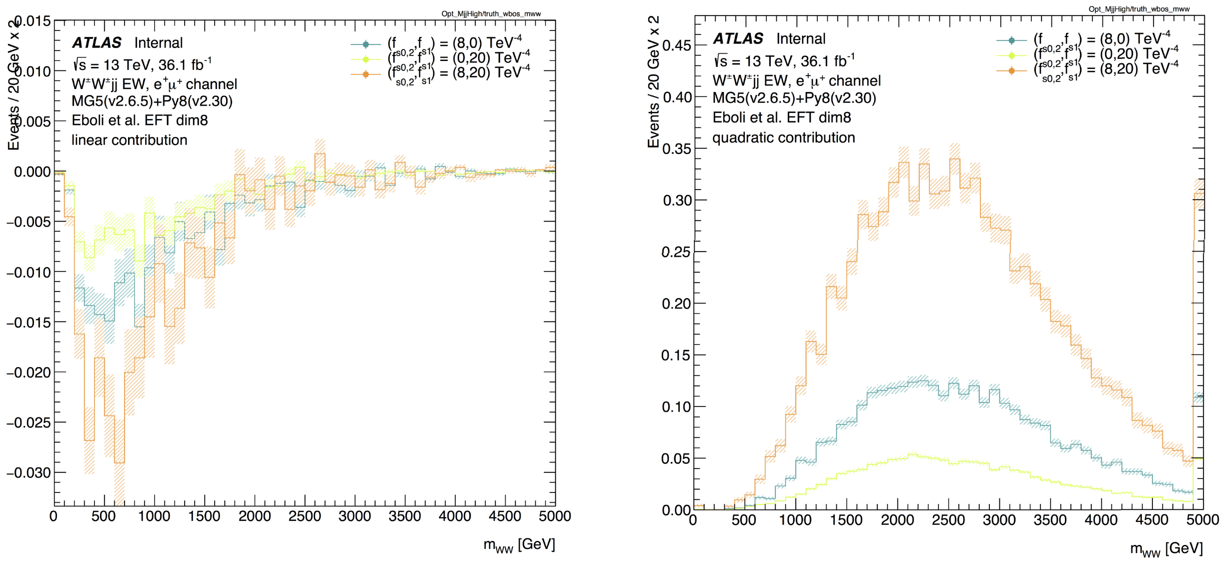

(a) $m_{ll\nu\nu}^{truth} \equiv m_{WW}$ interference term only

(b) $m_{ll\nu\nu}^{truth} \equiv m_{WW}$ quadratic term only

Figure 4.6: Kinematic distribution of the truth level variable $m_{ll\nu\nu}^{truth}$ (equivalent to the m_{WW} mentioned in the plots) for the parameters $f_{S,i}$. The two histograms only take the interference (a) or the quadratic (b) contributions into account.[21]

Table 4.2: Comparison between the $\pm 2\,\sigma$ limits for each operator determined by [2] and in this thesis for ssWW only and ssWW combined with WZ. The limits decrease by up to 16.7 % for the new EFT sample used here, but when including WZ EFTs only by maximal 6.8 %, even increasing by up to 4.5 %.

	$\pm 2\sigma_{previous}$		$\pm 2\sigma$ ssWW SR		$\pm 2\sigma$ combi SR	
M0	-5.08	5.02	-4.506	4.421	-4.32	4.495
M1	-7.69	8.21	-6.729	7.233	-6.471	7.387
M7	-11.77	11.24	-10.339	9.978	-	-
S0	-6.37	6.59	-5.899	6.112	-	-
S1	-25.52	26.25	-23.542	24.295	-22.406	25.092
T0	-0.47	0.5	-0.401	0.417	-0.373	0.436
T1	-0.22	0.24	-0.185	0.212	-0.184	0.211
T2	-0.71	0.89	-0.591	0.763	-0.588	0.759

of the limits when including WZ EFTs in the SR arises from the cancellation of yields: the numbers listed for interference and quadratic term in the cutflow tables are added to the yields from the SM prediction: a negative yield means destructive interference between the operator and the SM, so if the EFT would be realized in nature that would reduce the SM cross section. A cancellation of yields when adding ssWW and WZ interference or quadratic contributions means a smaller change in the SM predicted yields. That is why the combined fits in the SR did not improve the limits of the EFT coefficients significantly. Validity ranges for the operators M0, T1 and T2 where found to only improved a little bit compared to the ssWW only fits, in the case of M1 no change was found, the validity range for T0 decreases a little bit (compare Table 4.1).

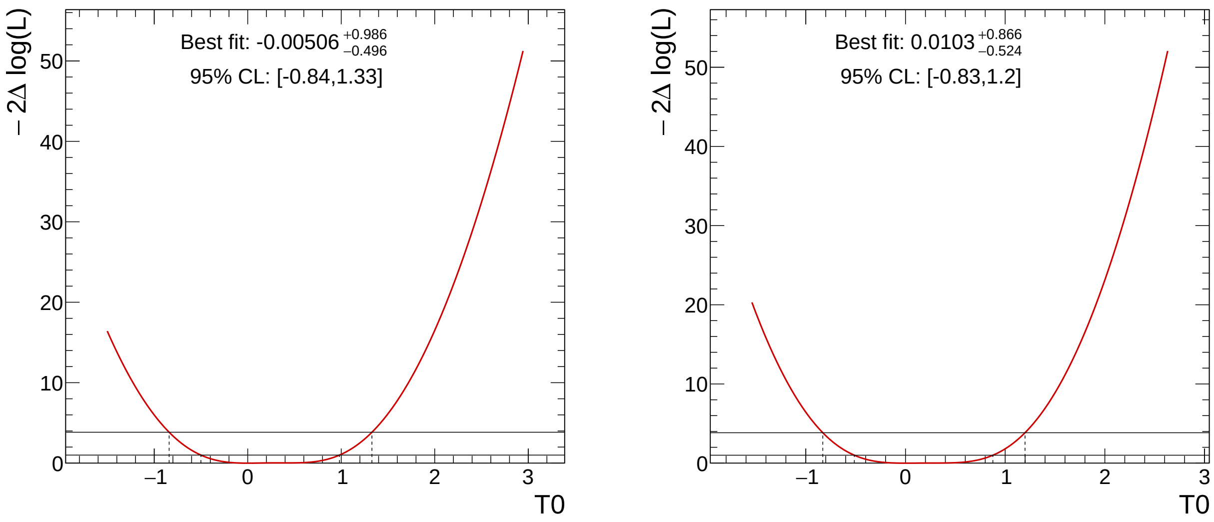

(a) $E_c = 1\,\mathrm{TeV}$ **(b)** $E_c = 1.5\,\mathrm{TeV}$

Figure 4.7: Negative maximum likelihood for the operator T0 for both ssWW and WZ combined in the SR (output from EFTfun tool).

5 Statistical limits in WZ control region

According to the yields (Table 3.1) and due to the selection criteria applied in the SR there are not a lot of WZ events to be found in the ssWW signal region. This section takes a look at a WZ control region (CR), where the yields for WZ are much higher (the ones for ssWW a lot lower of course) to extract the 1 and $2\,\sigma$ limits for all operators for which WZ EFT samples where available (all except S0, M7).

5.1 Construction of the WZ control region

After all the selection criteria are applied for the ssWW signal region, the background is dominated by the process of $W^{\pm}Z \rightarrow l^{\pm}\nu l^{\pm}l^{\mp}jj$. This may happen because one Z decay lepton is outside the detector acceptance region or it simply stays unidentified. Constructing a control region for background processes is often used to normalise its contribution in the signal region. Here the the idea is to use the yields from the CR as additional data, to improve the EFT limits for the combined fit of ssWW and WZ EFTs in a combined region SR+CR.
The construction of the WZ control region is described in more detail in [8], the most important selection criterion is that instead of being vetoed out, a third lepton is required, but it is allowed to have a smaller transverse momentum than the other two. The other criteria include further restrictions on other processes containing Z bosons and are otherwise fairly similar to the SR.
As can be seen in Table 5.1 and in the histogram Figure 5.1 the WZ control region indeed contains loads of WZ VBS events, and very few from ssWW. Like in the comparison for the signal region, there is a normalisation difference between the samples. The yields from the WZ EFT sample are in good agreement with those from the nominal sample. Since there are nearly no ssWW events to be found in this region, the fits will only be done for the WZ EFTs and neither for ssWW (since those results would be quite unreliable) nor the combination of both (since that would look approximately the same as for WZ alone).
In order to be able to compare results from SR and CR we will continue to use the dilepton invariant mass m_{ll}, which now evaluates the two leptons with the highest energy.

5.2 EFT limits for WZ in WZ CR

The logarithmic maximum likelihood scans for this scenario presented two familiar behaviours: T1 (Figure 5.3b) has a double minimum, which becomes quite small for higher energy clippings. The same asymmetry without double minimum is observed in the scans for T2. The $\pm 2\,\sigma$ values reflect these asymmetries: the absolute values of the $+2\,\sigma$ are all bigger than the $-2\,\sigma$ (Table 8.22, Table 8.23).

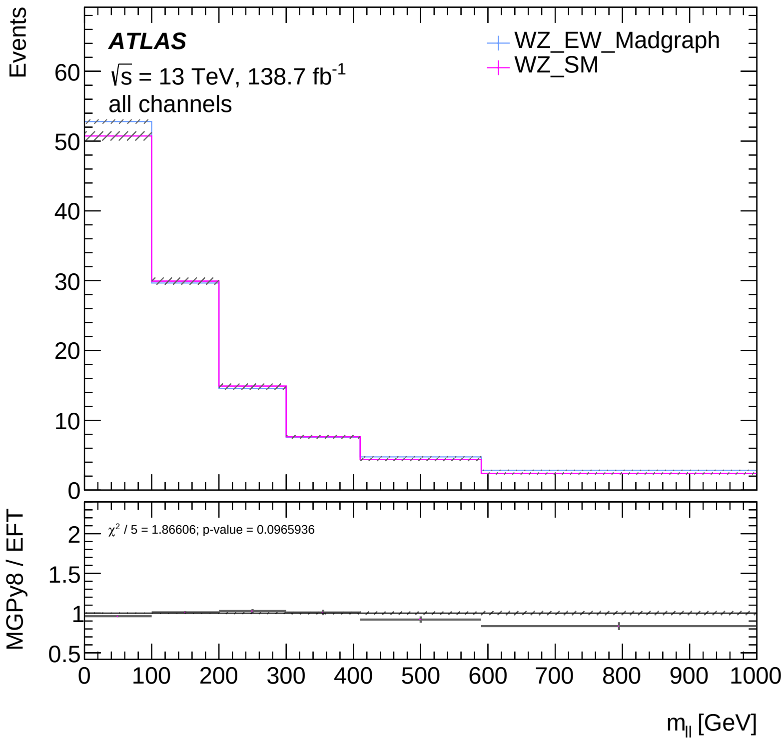

Figure 5.1: Kinematic distribution of m_{ll} in the WZ control region, comparing WZ_EW_Madgraph and WZ_SM from Table 5.1.

Table 5.1: Yield comparison between EFT sample and the support note ([8]) in the WZ control region; the left column includes statistical uncertainties on MC estimations, the right column shows statistical, theory, and experimental systematic uncertainties.

	all	VBS support note
ssWW_EW6_Madgraph	0.030 ± 0.006	$0.030 \pm 0.000 \pm 0.011 \pm 0.006$
ssWW_sm_sm	0.029 ± 0.022	
ssWW_QCD	0.006 ± 0.002	$0.006 \pm 0.002 \pm 0.005 \pm 0.001$
ssWW_Int	0.002 ± 0.001	$0.002 \pm 0.001 \pm 0.001 \pm 0.000$
WZ_QCD	733.845 ± 2.477	821.2 ± 2.6
WZ_EW_Madgraph	112.166 ± 0.448	141.4 ± 0.5
WZ_SM	109.956 ± 0.962	
Vgamma	20.242 ± 17.027	$9.589 \pm 2.640 \pm 0.000 \pm 4.428$
OtherPrompt	28.541 ± 0.471	$36.382 \pm 0.466 \pm 0.000 \pm 9.323$
ChargeFlip	5.805 ± 1.321	
NonPrompt	0.509 ± 0.255	

For the other operators the asymmetric behaviour appears to be mirrored compared to scans in the SR: as can be seen exemplary in Figure 5.3a the curve is flatter on the left side. When only looking at the cutflow table this seems to be unrelated to the sign of the interference term, but one idea would be to compare the histograms in the signal and control region binwise for each clipping and operator and to check whether the interference terms with smaller uncertainties contribute negative or positive values to the yield. For the operator T0 very high interference yields were found in the CR Table 8.5. One would expect the $\pm 2\,\sigma$ range to become a lot smaller for a yield that high, but taking the very big uncertainty into account this is not the case. The EFTfun tool considers those uncertainties when calculating the limits on the EFT operators, which should be the reason behind the very unspectacular change in the limits for T0 when comparing SR and CR. This consideration is further illustrated by the two histograms in Figure 5.2. Overall, when only looking at the numbers, the WZ $\pm 2\,\sigma$ ranges have improved compared to those in the signal region, as would be expected. Looking at the clipping scans Figure 8.2b, Figure 8.4b, Figure 8.7b, Figure 8.9b, Figure 8.11b, Figure 8.13b and the maximum validities in Table 4.1 no prominent deviation from the previous fits is noted: for S1 the $\pm 1.2\,\sigma$s continue to be located outside the unitarity bound making it impossible to find a validity range for this operator. The validity ranges for M1, T0, T2 stay close to previously found limits, the maximum validity for T1 is a little lower than for ssWW and the combination of ssWW and WZ in the SR, and for M0 a higher maximum validity is found.

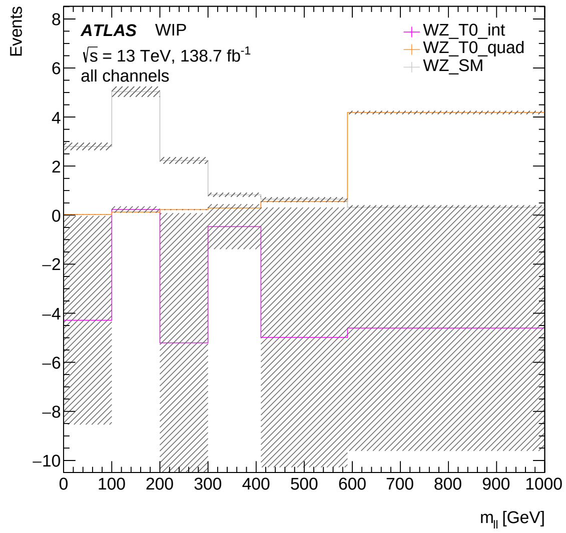

(a) SR

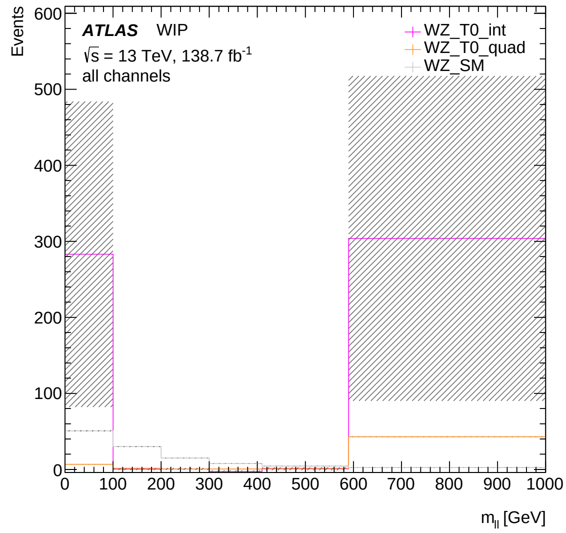

(b) CR

Figure 5.2: Histograms for the operator T0 showing the WZ EFT predictions for T0 interference and quadratic contribution as well as the SM prediction in the signal and control region without any clipping. For display purposes the operator T0 has an coefficient $\frac{c_n}{\Lambda^4} = 2.4\,\mathrm{TeV}^{-1}$ for the WZ sample.

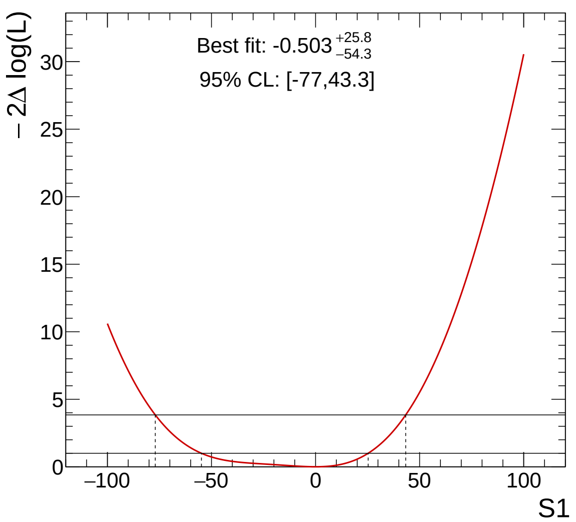

(a) S1 in CR at clipping $E_c = 1\,\mathrm{TeV}$

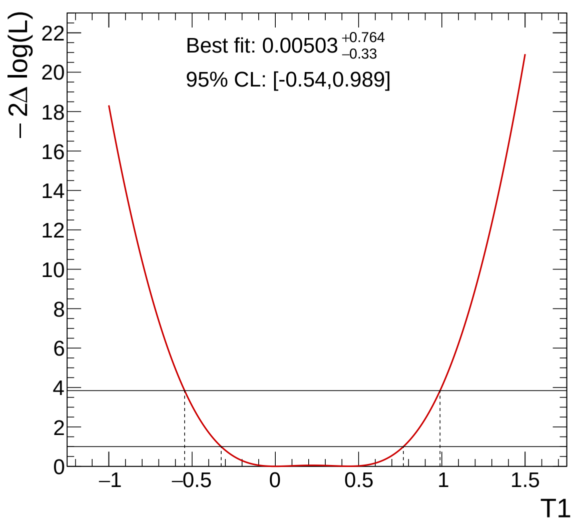

(b) T1 in CR at clipping $E_c = 1\,\mathrm{TeV}$

Figure 5.3: Negative maximum likelihood for the operators S1 and T1 in the control region (output from EFTfun tool).

6 Summary and Outlook

The objective of this thesis was to test how the validity ranges for the dimension-8 operators introduced in subsection 2.2 change when considering WZ background effects for the description of the VBS process of same sign $W^{\pm}W^{\pm}$ scattering in the framework of effective field theories. 95 % confidence level intervals ($\pm 2\,\sigma$ ranges) where extracted for five different clipping values (1, 1.5, 2 and 5 TeV and ∞ (no clipping)) in four different scenarios:

i fitting ssWW EFT samples in the ssWW signal region - these results where compared to the results from [2] and where found to be considerably lower;

ii fitting WZ EFT samples in the SR was not very successful, but information on different fit behaviours and their origin was gained;

iii from the fit of WZ in the WZ control region better limits where gained than in the SR;

iv fitting both ssWW and WZ in the SR improved the limits from scenario i) only for the operators M1, T1 and T2, for the others the $\pm 2\,\sigma$ increased, those for M0 increased for most clipping values.

Validity ranges for each operator were determined from the clipping plots in each of the scenarios for each operator separately. For S1 it was not possible to find a validity range in any fitting scenario, and due to missing samples M7 and S0 could only be evaluated for scenario i).
It was found that when combining the WZ and ssWW EFT samples and fitting them in the SR, the interference terms partially cancel each other out. This would mean that a possible deviation from the SM predicted cross section that could be detected would be smaller when only looking at the SR and considering background effects. Therefore, a scenario worth investigating would be to combine the signal and control region and do a fit of the combination of ssWW WZ. This might lead to more reliable results, since the combined region contains more data.
Depending on the tendency that emerges from this combined region it could be worth doing a new bin optimization for both regions.
This thesis evaluated the limits of one operator at a time, considering only the interference between the operator and the SM. More realistic results would be obtained by combined fits of multiple operators considering the cross terms in the effective Lagrangian. Last but not least this thesis only included statistical uncertainties. Considering systematic uncertainties will most likely have an impact on the $\pm 2\,\sigma$ limits, too.

Erklärung

Hiermit erkläre ich, dass ich diese Arbeit im Rahmen der Betreuung am Institut für Kern- und Teilchenphysik ohne unzulässige Hilfe Dritter verfasst und alle Quellen als solche gekennzeichnet habe.

Franziska Reichl
Dresden, August 2022

7 References

[1] E. Mobs: The CERN accelerator complex in 2019. In: *The CERN accelerator complex - August 2018* CERN-GRAPHICS-2019-002 (). URL: https://cds.cern.ch/record/2684277.

[2] P. M. Muller: Study of Sensitive Variables for dim-8 EFT Operators in Same Charge WWjj Scattering. PhD thesis. Technische Universitaet Dresden (DE), 4.04.2022. URL: http://cds.cern.ch/record/2805938/?ln=de.

[3] C. Bittrich: Evidence for Scattering of Electroweak Gauge Bosons in the $W
\pm Z$ Channel with the ATLAS Detector at the Large Hadron Collider. PhD thesis. Dresden, Tech. U, 27.05.2020. URL: https://cds.cern.ch/record/2719126.

[4] S. Todt: Investigation of mass reconstruction techniques for resonances in the scattering of $W
±*W*
±\to W
±*W*
±$*attheLHC*. PhD thesis. Dresden, Tech. U, 11.03.2015. URL: https://cds.cern.ch/record/2000966.

[5] Joao Pequenao: *Computer generated image of the whole ATLAS detector*. URL: https://cds.cern.ch/record/1095924#.

[6] C. Degrande, N. Greiner, W. Kilian, O. Mattelaer, H. Mebane, T. Stelzer, S. Willenbrock, and C. Zhang: Effective field theory: A modern approach to anomalous couplings. In: *Annals of Physics* 335 (2013), pp. 21–32. ISSN: 0003-4916. DOI: 10.1016/j.aop.2013.04.016. URL: https://www.sciencedirect.com/science/article/pii/S0003491613000894.

[7] Raquel Gomez-Ambrosio: Studies of Gauge Couplings at LHC: the Effective Field Theory Approach. PhD thesis. Unpublished, 2017. DOI: 10.13140/RG.2.2.23472.87049.

[8] M. Queitsch-Maitland, A. S. Tegetmeier, T. Herrmann, C. Mwewa, M. V. Stange, C. P. Becot, J. A. Fernandez Pretel, F. He, J. Manjarres, S. Todt, B. Heinemann, M.-A. Pleier, O. Kuprash, R. Ospanov, S. Solomon, M. Kobel, J. Zhu, C. P. Klimanek, C. Bittrich, and K. Potamianos: *Support note for measurement of fiducial and differential $W\pm W\pm jj$ production cross-sections at $\sqrt{}$ = 13 TeV using the full Run-2 dataset*. URL: https://cds.cern.ch/record/2790652/.

[9] O. J. P. Éboli and M. C. Gonzalez–Garcia: Classifying the bosonic quartic couplings. In: *Physical Review D* 93.9 (2016), p. 093013. ISSN: 2470-0010. DOI: 10.1103/PhysRevD.93.093013.

[10] E. S. Da Almeida, O. J. P. Éboli, and M. C. Gonzalez–Garcia: Unitarity constraints on anomalous quartic couplings. In: *Physical Review D* 101.11 (2020). ISSN: 2470-0010. DOI: 10.1103/PhysRevD.101.113003.

[11] M. Erdmann, T. Hebbeker, and A. Schmidt: *Statistische Methoden in der Experimentalphysik*. Person Studium - Physik. Hallbergmoos: Pearson, 2020. ISBN: 9783863268886. DOI: Martin. URL: https://ebookcentral.proquest.com/lib/kxp/detail.action?docID=6148211.

[12] *EFT tools / EFTfun · GitLab*. 21.08.2022. URL: https://gitlab.cern.ch/eft-tools/eft-fun.

[13] Public Books: *Asimov's Empire, Asimov's Wall | Public Books*. 2020. URL: https://web.archive.org/web/20200109111535/https://www.publicbooks.org/asimovs-empire-asimovs-wall/.

[14] G. Cowan, K. Cranmer, E. Gross, and O. Vitells: Asymptotic formulae for likelihood-based tests of new physics. In: *The European Physical Journal C* 71.2 (2011). ISSN: 1434-6052. DOI: 10.1140/epjc/s10052-011-1554-0. URL: https://arxiv.org/pdf/1007.1727.

[15] B. Cabouat and T. Sjöstrand: Some dipole shower studies. In: *The European physical journal. C, Particles and fields* 78.3 (2018), p. 226. ISSN: 1434-6044. DOI: 10.1140/epjc/s10052-018-5645-z. URL: https://arxiv.org/pdf/1710.00391.

[16] A. Buckley, J. Butterworth, S. Gieseke, D. Grellscheid, S. Höche, H. Hoeth, F. Krauss, L. Lönnblad, E. Nurse, P. Richardson, S. Schumann, M. H. Seymour, T. Sjöstrand, P. Skands, and B. Webber: General-purpose event generators for LHC physics. In: *Physics Reports* 504.5 (2011), pp. 145–233. ISSN: 0370-1573. DOI: 10.1016/j.physrep.2011.03.005. URL: https://www.sciencedirect.com/science/article/pii/S0370157311000846.

[17] J. Alwall, R. Frederix, S. Frixione, V. Hirschi, F. Maltoni, O. Mattelaer, H.-S. Shao, T. Stelzer, P. Torrielli, and M. Zaro: The automated computation of tree-level and next-to-leading order differential cross sections, and their matching to parton shower simulations. In: *Journal of High Energy Physics* 2014.7 (2014). DOI: 10.1007/JHEP07(2014)079. URL: https://arxiv.org/pdf/1405.0301.

[18] B. E. Lindquist, D. Iliadis, M.-A. Pleier, K. Lohwasser, A. Bocci, L. Di Ciaccio, V. Kouskoura, M. Kobel, S. Li, and Y. Wu: *Recommendations from the Anomalous Gauge Coupling Taskforce*. URL: https://cds.cern.ch/record/2261444/.

[19] A. M. Sirunyan et al.: Measurements of production cross sections of WZ and same-sign WW boson pairs in association with two jets in proton-proton collisions at s=13TeV. In: *Physics Letters B* 809 (2020), p. 135710. ISSN: 03702693. DOI: 10.1016/j.physletb.2020.135710. URL: https://arxiv.org/pdf/2005.01173.

[20] *Common Analysis Framework - Online Documentation*. 16.06.2021. URL: https://atlas-caf.web.cern.ch/.

[21] D. Sampsonidou, T. Herrmann, J. Manjarres, S. Todt, H. Mildner, M. Kobel, C. Petridou, and E. Kasimi: *aQGC re-interpretation of ssWW and WZjj*. URL: https://cds.cern.ch/record/2791985.

List of Figures

List of Tables

8 Appendix

Table 8.1: Unitarity constrains on the Wilson coefficients relevant to this thesis (when setting only one coefficient not to zero) as found in [10].

$\lvert f_{M0}\rvert$	$\frac{32}{\sqrt{6}}\pi s^{-2}$
$\lvert f_{M1}\rvert$	$\frac{128}{\sqrt{6}}\pi s^{-2}$
$\lvert f_{M7}\rvert$	$\frac{256}{\sqrt{6}}\pi s^{-2}$
$\lvert f_{S0}\rvert$	$32\pi s^{-2}$
$\lvert f_{S1}\rvert$	$\frac{96}{7}\pi s^{-2}$
$\lvert f_{T0}\rvert$	$\frac{12}{5}\pi s^{-2}$
$\lvert f_{T1}\rvert$	$\frac{24}{5}\pi s^{-2}$
$\lvert f_{T2}\rvert$	$\frac{96}{13}\pi s^{-2}$

Table 8.2: Cutflow for M0 in ssWW SR and CR (plus cuts) including the ratios between interference and quadratic term for each ssWW, WZ, and the combination of both.

		ssWW		WZ		combi		ssWW	WZ	combi
	E_c [TeV]	M0_int	M0_quad	M0_int	M0_quad	M0_int	M0_quad	int/quad	int/quad	int/quad
SR	1	1.016 ± 0.059	1.689 ± 0.029	-4.284 ± 5.019	4.354 ± 0.086	-3.268	6.043	0.602	-0.984	-0.541
	1.5	1.135 ± 0.073	3.151 ± 0.040	-9.665 ± 5.851	5.193 ± 0.094	-8.530	8.343	0.360	-1.861	-1.022
	2	1.185 ± 0.080	5.373 ± 0.052	-12.259 ± 6.169	5.950 ± 0.101	-11.074	11.322	0.221	-2.061	-0.978
	5	1.223 ± 0.082	14.509 ± 0.086	-11.385 ± 6.222	7.035 ± 0.110	-10.162	21.544	0.084	-1.618	-0.472
	∞	1.223 ± 0.082	14.993 ± 0.087	-11.385 ± 6.222	7.039 ± 0.110	-10.162	22.032	0.082	-1.617	-0.461
CR	1	0.000 ± 0.000	0.001 ± 0.001	-7.998 ± 75.181	58.956 ± 0.321	-7.998	58.957	0.173	-0.136	-0.136
	1.5	0.000 ± 0.000	0.001± 0.001	-15.147 ± 75.389	62.905 ± 0.332	-15.147	62.906	0.133	-0.241	-0.241
	2	0.000 ± 0.000	0.001 ± 0.001	-14.955 ± 75.396	67.189 ± 0.343	-14.954	67.191	0.070	-0.223	-0.223
	5	0.000 ± 0.000	0.003 ± 0.001	-14.409 ± 75.398	74.076 ± 0.360	-14.409	74.078	0.035	-0.195	-0.195
	∞	0.000 ± 0.000	0.003 ± 0.001	-14.408 ± 75.398	74.141 ± 0.361	-14.408	74.144	0.033	-0.194	-0.194

Table 8.3: Cutflow for M1 in ssWW SR and CR (plus cuts) including the ratios between interference and quadratic term for each ssWW, WZ, and the combination of both (referred to in subsection 4.2).

		ssWW		WZ		combi		ssWW	WZ	combi
	E_c [TeV]	M1_int	M1_quad	M1_int	M1_quad	M1_int	M1_quad	int/quad	int/quad	int/quad
SR	1	-1.077 ± 0.039	1.950 ± 0.035	5.867 ± 2.730	1.763 ± 0.036	4.790	3.713	-0.552	3.328	1.290
	1.5	-1.600 ± 0.046	3.718 ± 0.049	4.740 ± 3.313	2.138 ± 0.040	3.140	5.856	-0.430	2.217	0.536
	2	-1.889 ± 0.050	6.535 ± 0.065	4.254 ± 3.350	2.449 ± 0.042	2.365	8.984	-0.289	1.737	0.263
	5	-2.149 ± 0.053	18.481 ± 0.110	4.256 ± 3.350	2.913 ± 0.046	2.107	21.394	-0.116	1.461	0.098
	∞	-2.150 ± 0.053	19.104 ± 0.112	4.256 ± 3.350	2.915 ± 0.046	2.106	22.018	-0.113	1.460	0.096
CR	1	-0.000 ± 0.000	0.001 ± 0.001	12.739 ± 12.723	27.828 ± 0.143	12.739	27.830	-0.223	0.458	0.458
	1.5	-0.000 ± 0.000	0.002 ± 0.001	15.386 ± 13.430	29.816 ± 0.148	15.386	29.817	-0.177	0.516	0.516
	2	-0.000 ± 0.000	0.004 ± 0.002	13.213 ± 13.668	31.882 ± 0.153	13.212	31.887	-0.111	0.414	0.414
	5	-0.001 ± 0.001	0.008 ± 0.002	14.385 ± 13.683	34.990 ± 0.161	14.385	34.998	-0.093	0.411	0.411
	∞	-0.001 ± 0.001	0.008 ± 0.002	14.385 ± 13.683	35.018 ± 0.161	14.384	35.027	-0.093	0.411	0.411

Table 8.4: Cutflow for S1 in ssWW SR and CR (plus cuts) including the ratios between interference and quadratic term for each ssWW, WZ, and the combination of both.

		ssWW		WZ		combi		ssWW	WZ	combi
	E_c [TeV]	S1_int	S1_quad	S1_int	S1_quad	S1_int	S1_quad	int/quad	int/quad	int/quad
SR	1	-0.590 ± 0.029	0.562 ± 0.011	-0.960 ± 3.534	3.212 ± 0.061	-1.550	3.774	-1.050	-0.299	-0.411
	1.5	-0.746 ± 0.034	1.433 ± 0.017	-1.076 ± 3.535	4.095 ± 0.069	-1.822	5.528	-0.521	-0.263	-0.330
	2	-0.798 ± 0.036	2.652 ± 0.024	0.013 ± 3.594	4.796 ± 0.075	-0.785	7.448	-0.301	0.003	-0.105
	5	-0.848 ± 0.037	6.141 ± 0.036	0.135 ± 3.596	5.367 ± 0.079	-0.713	11.508	-0.138	0.025	-0.062
	∞	-0.849 ± 0.037	6.219 ± 0.036	0.135 ± 3.596	5.367 ± 0.079	-0.714	11.586	-0.137	0.025	-0.062
CR	1	-0.000 ± 0.001	0.000 ± 0.000	20.581 ± 19.065	47.505 ± 0.239	20.581	47.505	-2.620	0.433	0.433
	1.5	-0.000 ± 0.001	0.000 ± 0.000	21.677 ± 19.589	51.664 ± 0.249	21.676	51.664	-0.961	0.420	0.420
	2	-0.000 ± 0.001	0.002 ± 0.001	14.583 ± 19.848	55.417 ± 0.258	14.583	55.419	-0.110	0.263	0.263
	5	-0.000 ± 0.001	0.002 ± 0.001	13.035 ± 19.921	59.102 ± 0.267	13.035	59.104	-0.223	0.221	0.221
	∞	-0.000 ± 0.001	0.002 ± 0.001	13.035 ± 19.921	59.112 ± 0.267	13.035	59.114	-0.223	0.221	0.220

Table 8.5: Cutflow for T0 in ssWW SR and CR (plus cuts) including the ratios between interference and quadratic term for each ssWW, WZ, and the combination of both.

		ssWW		WZ		combi		ssWW	WZ	combi
	E_c [TeV]	T0_int	T0_quad	M0_int	T0_quad	T0_int	T0_quad	int/quad	int/quad	int/quad
	1	-0.495 ± 0.275	2.076 ± 0.032	-15.132 ± 8.468	3.243 ± 0.060	-15.628	5.319	-0.239	-4.666	-2.938
	1.5	-0.922 ± 0.276	3.029 ± 0.039	-14.445 ± 8.486	3.633 ± 0.063	-15.367	6.662	-0.304	-3.976	-2.307
SR	2	-1.194 ± 0.276	4.665 ± 0.048	-19.318 ± 10.004	4.123 ± 0.068	-20.512	8.789	-0.256	-4.685	-2.334
	5	-1.150 ± 0.393	15.536 ± 0.088	-19.319 ± 10.004	5.380 ± 0.077	-20.470	20.917	-0.074	-3.591	-0.979
	∞	-1.150 ± 0.393	16.680 ± 0.091	-19.319 ± 10.004	5.409 ± 0.078	-20.470	22.089	-0.069	-3.572	-0.927
	1	0.000 ± 0.000	0.000 ± 0.000	288.037 ± 204.124	42.607 ± 0.218	288.037	42.607	0.144	6.760	6.760
	1.5	-0.000 ± 0.000	0.001 ± 0.000	441.827 ± 255.150	44.431 ± 0.223	441.827	44.432	-0.081	9.944	9.944
CR	2	-0.000 ± 0.000	0.001 ± 0.001	585.706 ± 293.363	46.817 ± 0.229	585.706	46.818	-0.052	12.511	12.510
	5	-0.000 ± 0.000	0.002 ± 0.001	585.747 ± 293.363	53.284 ± 0.244	585.747	53.286	-0.024	10.993	10.992
	∞	-0.000± 0.000	0.002 ± 0.001	585.747 ± 293.363	53.467 ± 0.244	585.747	53.469	-0.024	10.955	10.955

Table 8.6: Cutflow for T1 in ssWW SR and CR (plus cuts) including the ratios between interference and quadratic term for each ssWW, WZ, and the combination of both.

		ssWW		WZ		combi		ssWW	WZ	combi
	E_c[TeV]	T1_int	T1_quad	T1_int	T1_quad	T1_int	T1_quad	int/quad	int/quad	int/quad
	1	-1.582 ± 0.022	2.165 ± 0.033	-0.291 ± 0.010	2.892 ± 0.052	-1.874	5.057	-0.731	-0.101	-0.370
	1.5	-2.518 ± 0.027	2.883 ± 0.038	-0.328 ± 0.010	3.244 ± 0.055	-2.846	6.127	-0.873	-0.101	-0.464
SR	2	-3.174 ± 0.030	4.503 ± 0.048	-0.344 ± 0.010	3.693 ± 0.058	-3.518	8.196	-0.705	-0.093	-0.429
	5	-4.030 ± 0.033	17.641 ± 0.095	-0.358 ± 0.010	4.894 ± 0.067	-4.389	22.535	-0.228	-0.073	-0.195
	∞	-4.036 ± 0.033	19.225 ± 0.099	-0.358 ± 0.010	4.919 ± 0.067	-4.394	24.144	-0.210	-0.073	-0.182
	1	-0.001 ± 0.000	0.000 ± 0.000	-16.536 ± 5.144	43.938 ± 0.205	-16.537	43.938	-2.190	-0.376	-0.376
	1.5	-0.001 ± 0.001	0.000 ± 0.000	-16.836 ± 5.144	45.567 ± 0.209	-16.838	45.568	-3.524	-0.369	-0.370
CR	2	-0.001 ± 0.001	0.000 ± 0.000	-17.006 ± 5.144	47.957 ± 0.214	-17.008	47.957	-4.342	-0.355	-0.355
	5	-0.001 ± 0.001	0.005 ± 0.002	-17.122 ± 5.144	54.912 ± 0.229	-17.123	54.917	-0.274	-0.312	-0.312
	∞	-0.001 ± 0.001	0.005 ± 0.002	-17.123 ± 5.144	55.094 ± 0.230	-17.124	55.100	-0.274	-0.311	-0.311

Table 8.7: Cutflow for T2 in ssWW SR and CR (plus cuts) including the ratios between interference and quadratic term for each ssWW, WZ, and the combination of both. (referred to in subsection 4.1).

		ssWW		WZ		combi		ssWW	WZ	combi
	E_c[TeV]	T2_int	T2_quad	T2_int	T2_quad	T2_int	T2_quad	int/quad	int/quad	int/quad
	1	-2.617 ± 0.033	2.672 ± 0.041	-0.233 ± 0.243	3.836 ± 0.072	-2.850	6.508	-0.979	-0.061	-0.438
	1.5	-4.325 ± 0.041	3.599 ± 0.048	-0.316 ± 0.243	4.370 ± 0.077	-4.641	7.969	-1.202	-0.072	-0.582
SR	2	-5.503 ± 0.045	5.543 ± 0.059	-0.361 ± 0.243	4.971 ± 0.082	-5.864	10.514	-0.993	-0.073	-0.558
	5	-7.019 ± 0.050	20.874 ± 0.115	-0.393 ± 0.243	6.452 ± 0.093	-7.412	27.326	-0.336	-0.061	-0.271
	∞	-7.026 ± 0.050	22.727 ± 0.120	-0.393 ± 0.243	6.499 ± 0.093	-7.419	29.226	-0.309	-0.060	-0.254
	1	-0.001 ± 0.000	0.000 ± 0.000	-7.810 ± 0.248	60.814 ± 0.289	-7.811	60.814	-2.861	-0.128	-0.128
	1.5	-0.001 ± 0.000	0.002 ± 0.001	-8.392 ± 0.249	63.116 ± 0.295	-8.393	63.118	-0.456	-0.133	-0.133
	2	-0.001 ± 0.001	0.002 ± 0.001	-8.695 ± 0.249	66.652 ± 0.303	-8.696	66.654	-0.666	-0.130	-0.130
	5	-0.003 ± 0.001	0.008 ± 0.002	-8.914 ± 0.249	76.011 ± 0.323	-8.917	76.020	-0.300	-0.117	-0.117
	∞	-0.003 ± 0.001	0.009 ± 0.003	-8.915 ± 0.249	76.242 ± 0.324	-8.917	76.251	-0.272	-0.117	-0.117

Table 8.8: Cutflow for M7 in ssWW SR (plus cuts) including the ratios between interference and quadratic term.

	E_c[TeV]	ssWW_sm_sm	ssWW_M7_int	ssWW_M7_quad	int/quad
SR	1	204.183 ± 1.755	0.568 ± 0.175	1.455 ± 0.025	0.390
	1.5	208.507 ± 1.774	0.773 ± 0.225	2.774 ± 0.034	0.279
	2	209.099 ± 1.777	1.081 ± 0.256	4.922 ± 0.046	0.220
	5	209.211 ± 1.777	1.252 ± 0.257	13.863 ± 0.077	0.090
	∞	209.211 ± 1.777	1.252 ± 0.257	14.352 ± 0.078	0.087
CR	1	0.029 ± 0.022	0.000 ± 0.001	0.000 ± 0.000	0.869
	1.5	0.029 ± 0.022	0.001 ± 0.001	0.000 ± 0.000	1.517
	2	0.029 ± 0.022	0.001 ± 0.001	0.001 ± 0.000	1.036
	5	0.029 ± 0.022	0.001 ± 0.001	0.002 ± 0.001	0.388
	∞	0.029 ± 0.022	0.001 ± 0.001	0.002 ± 0.001	0.388

Table 8.9: Cutflow for S0 in ssWW SR (plus cuts) including the ratios between interference and quadratic term.

	E_c[TeV]	ssWW_sm_sm	ssWW_S0_int	ssWW_S0_quad	int/quad
SR	1	204.183 ± 1.755	-1.066 ± 0.043	1.417 ± 0.027	-0.752
	1.5	208.507 ± 1.774	-1.331 ± 0.050	3.711 ± 0.043	-0.359
	2	209.099 ± 1.777	-1.435 ± 0.053	6.856 ± 0.059	-0.209
	5	209.211 ± 1.777	-1.504 ± 0.055	15.668 ± 0.089	-0.096
	∞	209.211 ± 1.777	-1.504 ± 0.055	15.884 ± 0.090	-0.095
CR	1	0.029 ± 0.022	-0.001 ± 0.001	0.000 ± 0.000	-2.206
	1.5	0.029 ± 0.022	-0.001 ± 0.001	0.001 ± 0.001	-0.851
	2	0.029± 0.022	-0.001 ± 0.001	0.003 ± 0.001	-0.357
	5	0.029± 0.022	-0.001 ± 0.001	0.005 ± 0.002	-0.196
	∞	0.029 ± 0.022	-0.001 ± 0.001	0.005 ± 0.002	-0.196

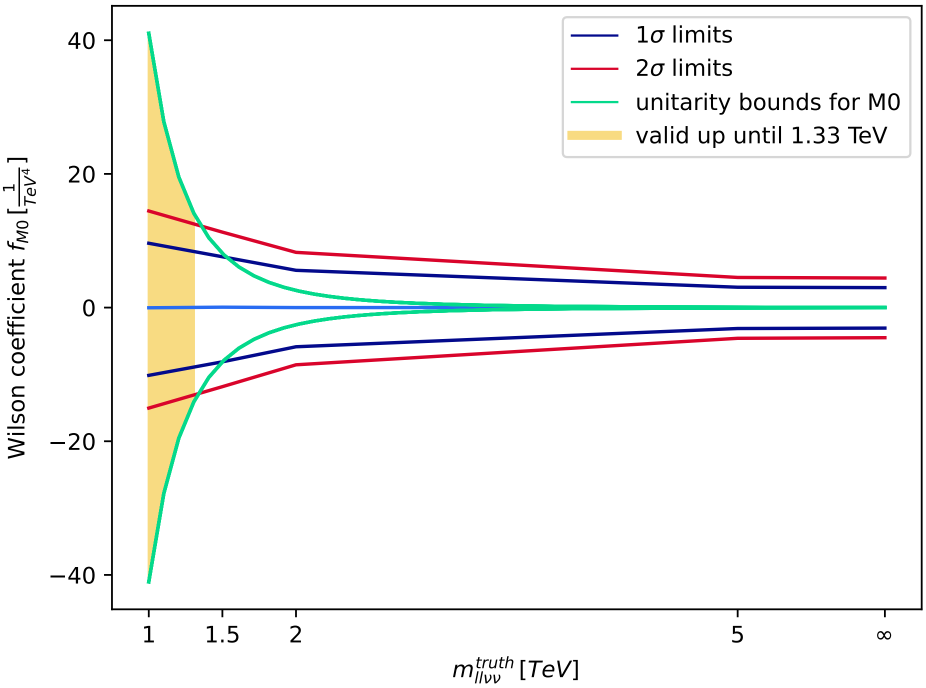

(a) ssWW in SR for operator M0

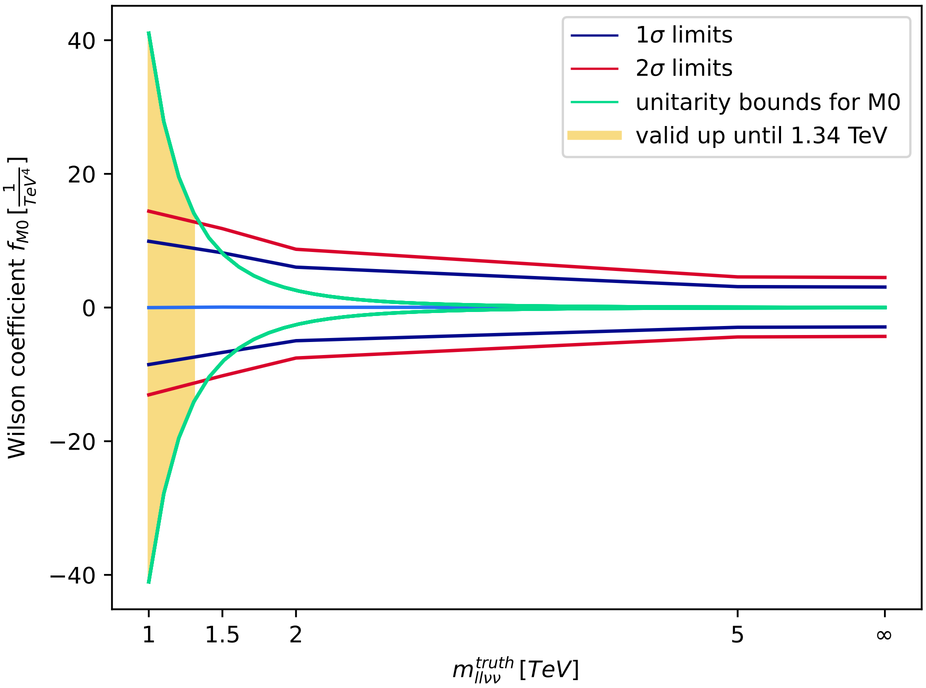

(b) combi ssWW+WZ in SR for operator M0

Figure 8.1: Clippping scans for the EFT operator M0, for ssWW (a), ssWW and WZ combined (b) in the SR.

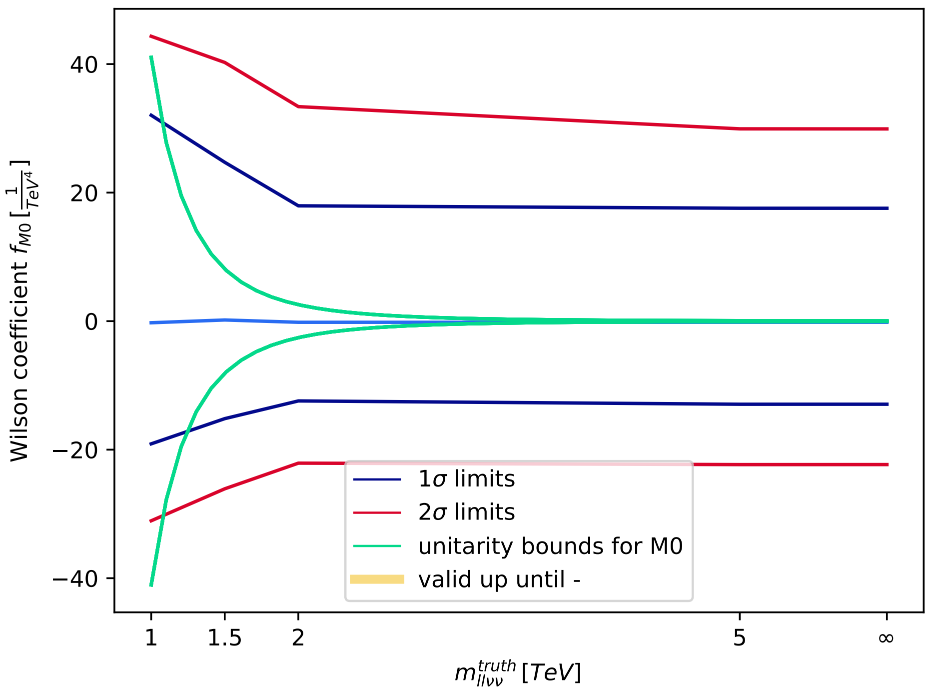

(a) WZ in SR for operator M0

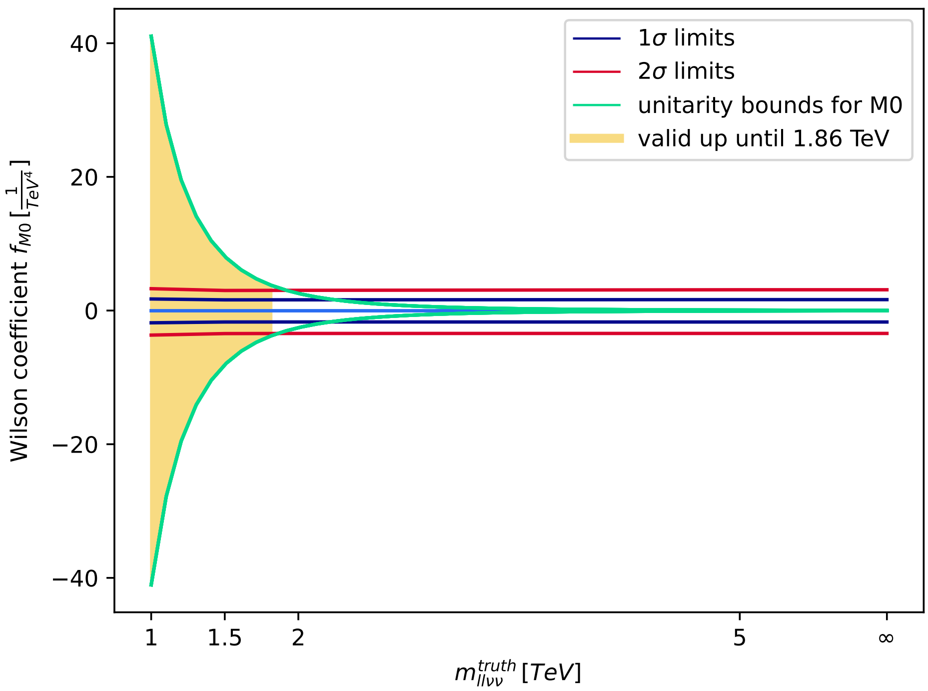

(b) WZ in CR for operator M0

Figure 8.2: Clippping scans for the EFT operator M0, for WZ in the ssWW SR (a) and the WZ control region (b).

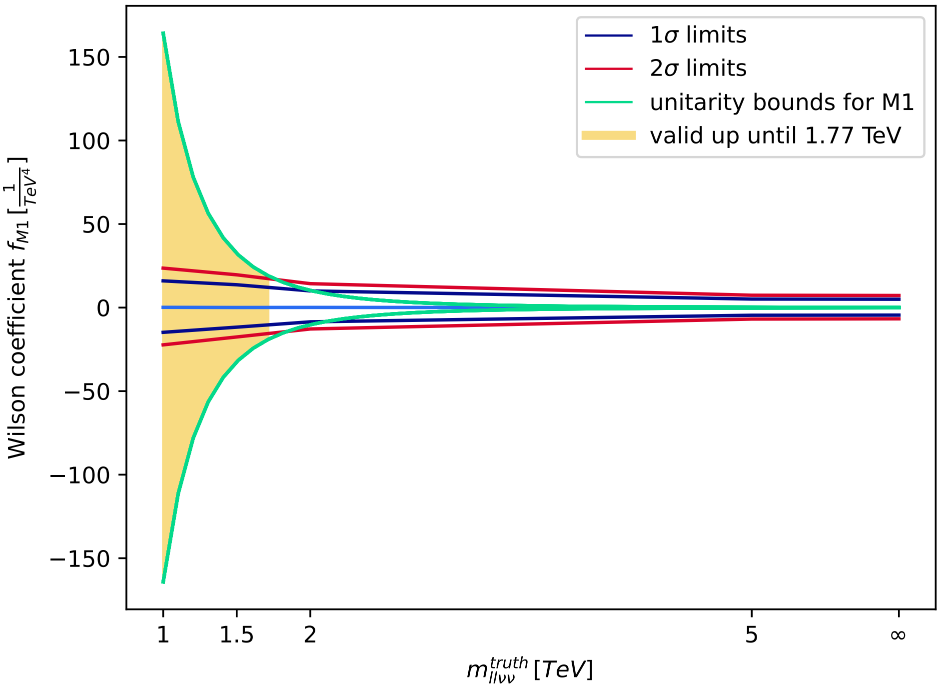

(a) ssWW in SR for operator M1

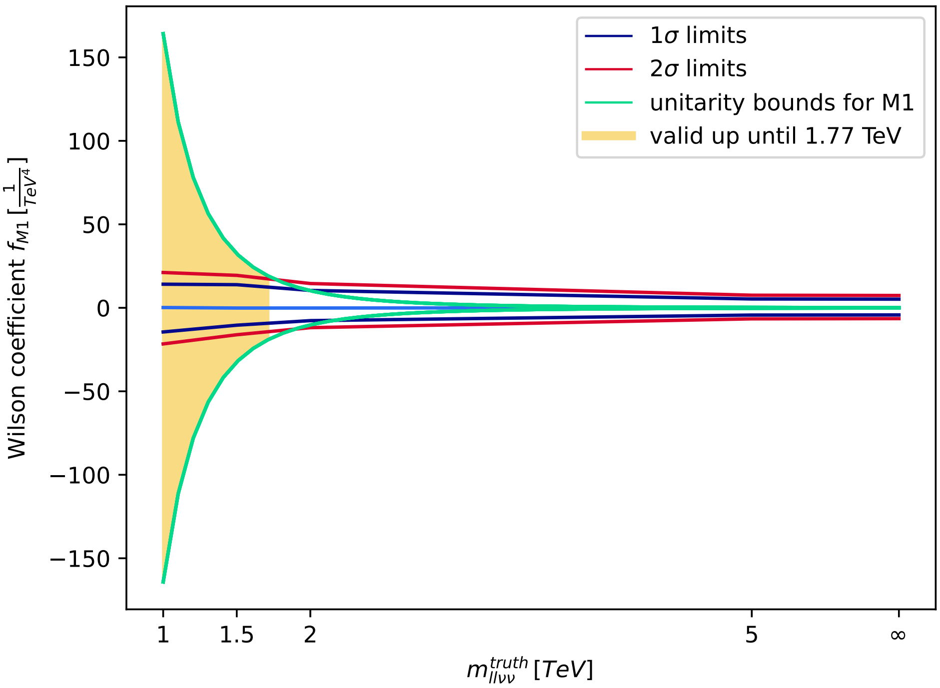

(b) combi ssWW+WZ in SR for operator M1

Figure 8.3: Clippping scans for the EFT operator M1, for ssWW (a), ssWW and WZ combined (b) in the SR.

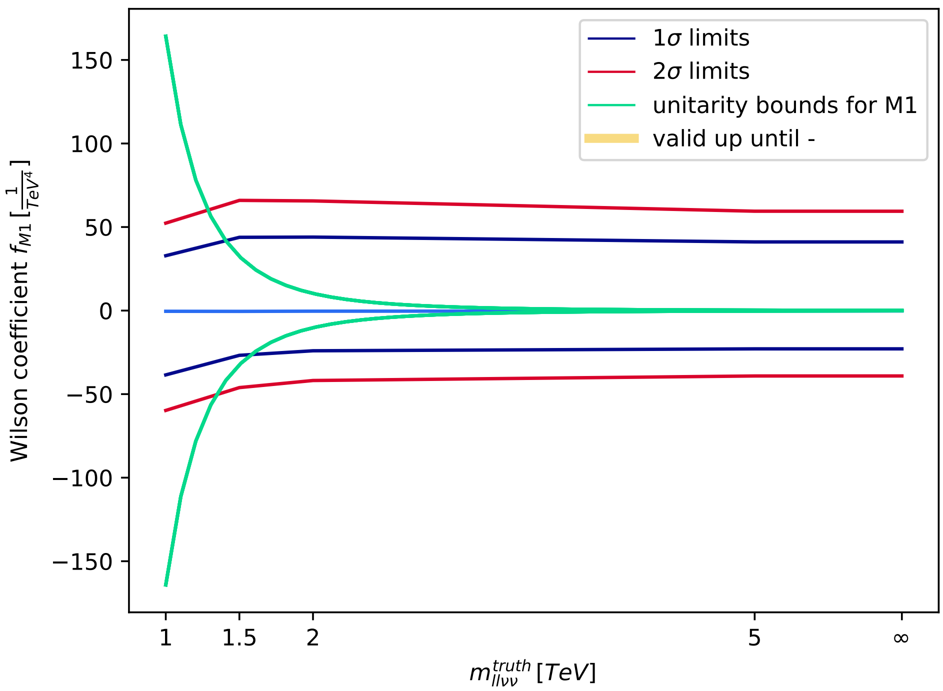

(a) WZ in SR for operator M1

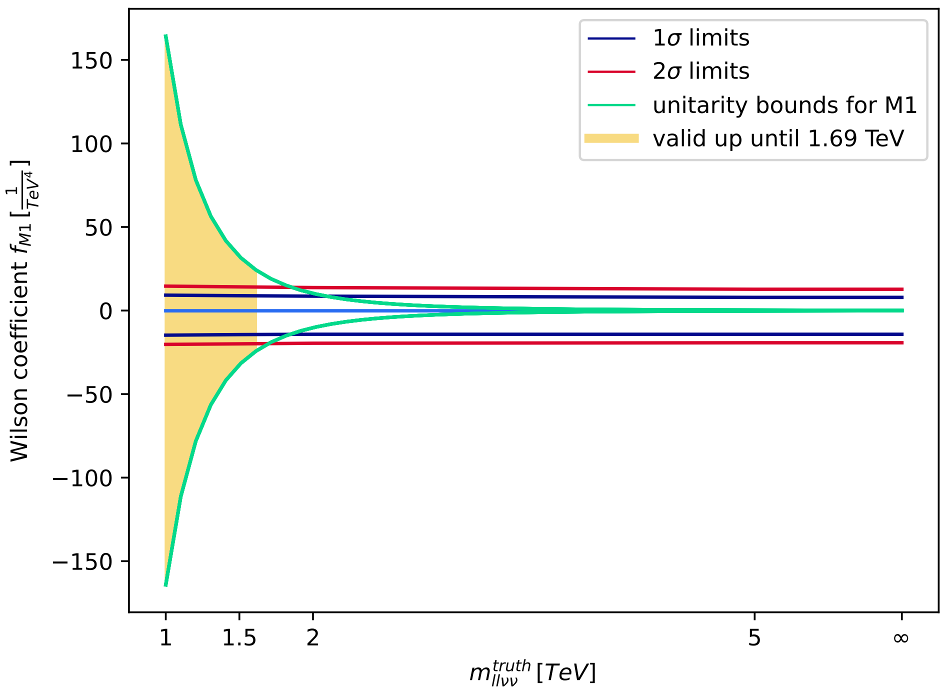

(b) WZ in CR for operator M1

Figure 8.4: Clippping scans for the EFT operator M1, for WZ in the ssWW SR (a) and the WZ control region (b).

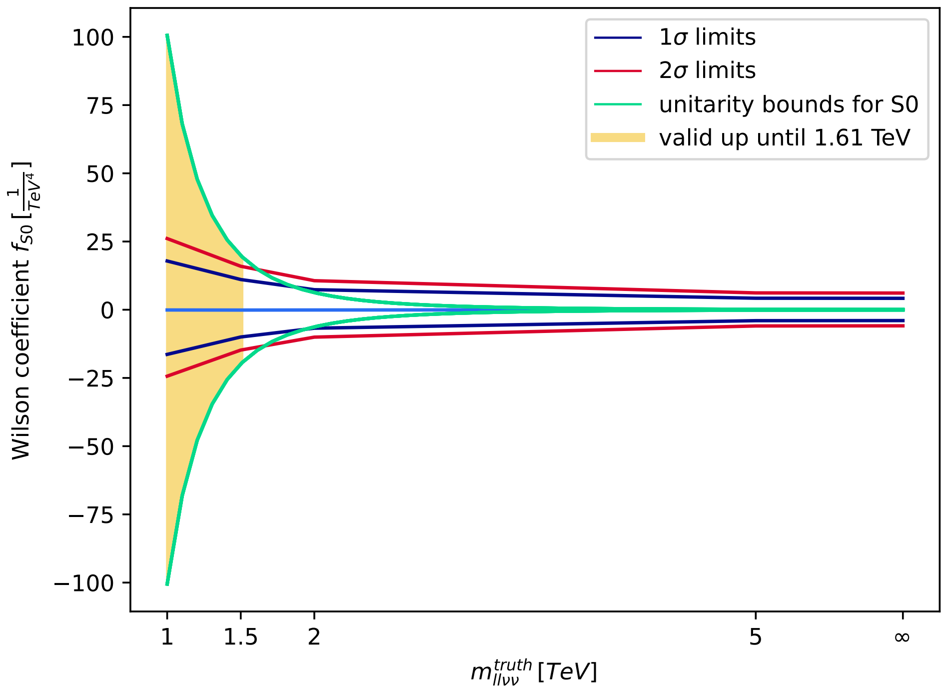

(a) ssWW in SR for operator S0

Figure 8.5: Clippping scan for the EFT operator S0 for ssWW in SR.

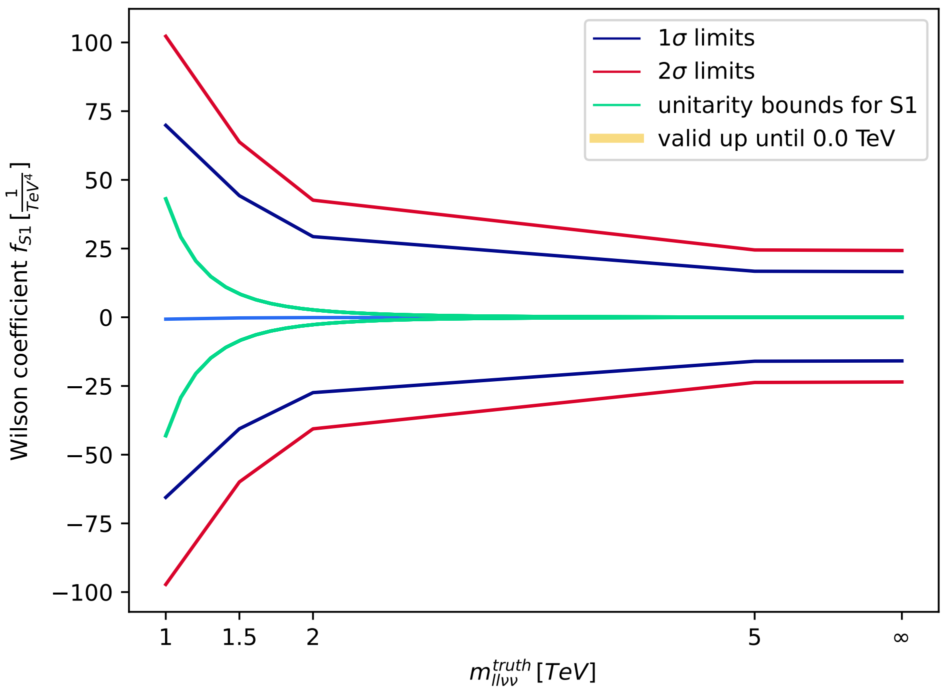

(a) ssWW in SR for operator S1

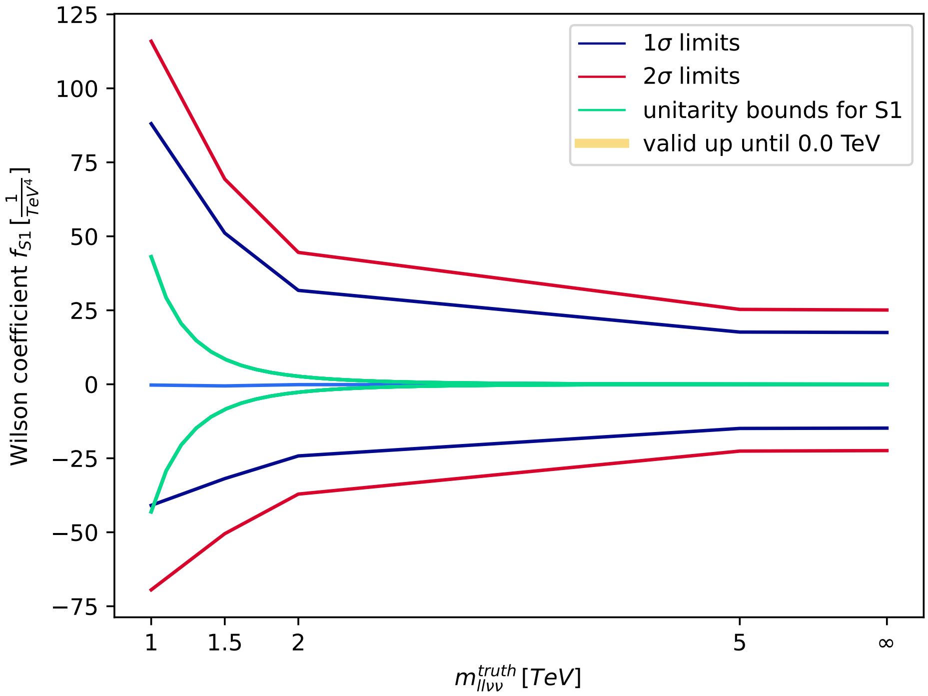

(b) combi ssWW+WZ in SR for operator S1

Figure 8.6: Clippping scans for the EFT operator S1, for ssWW (a), ssWW and WZ combined (b) in the SR.

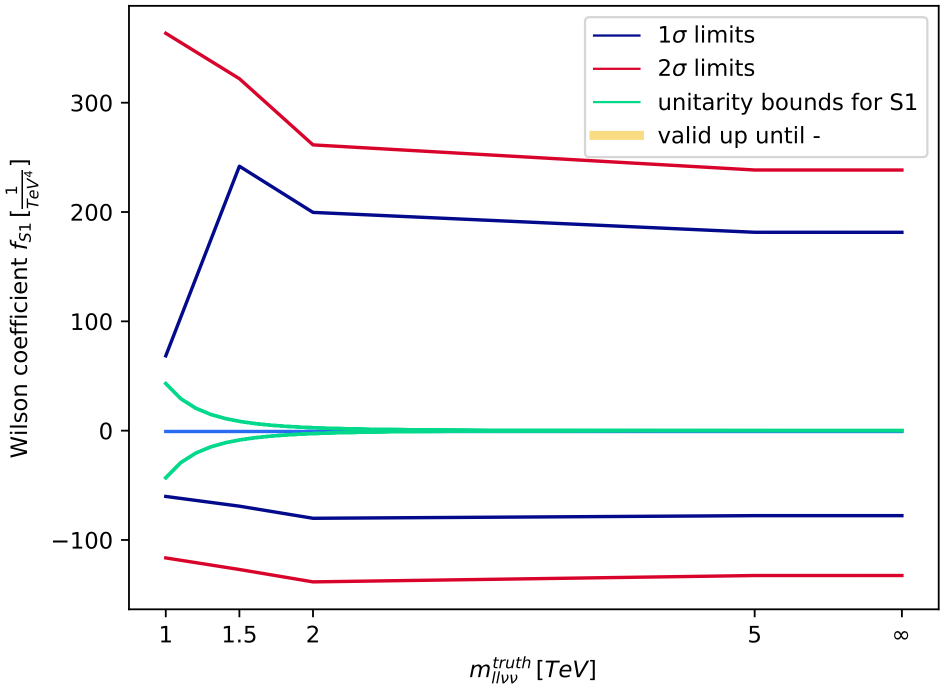

(a) WZ in SR for operator S1

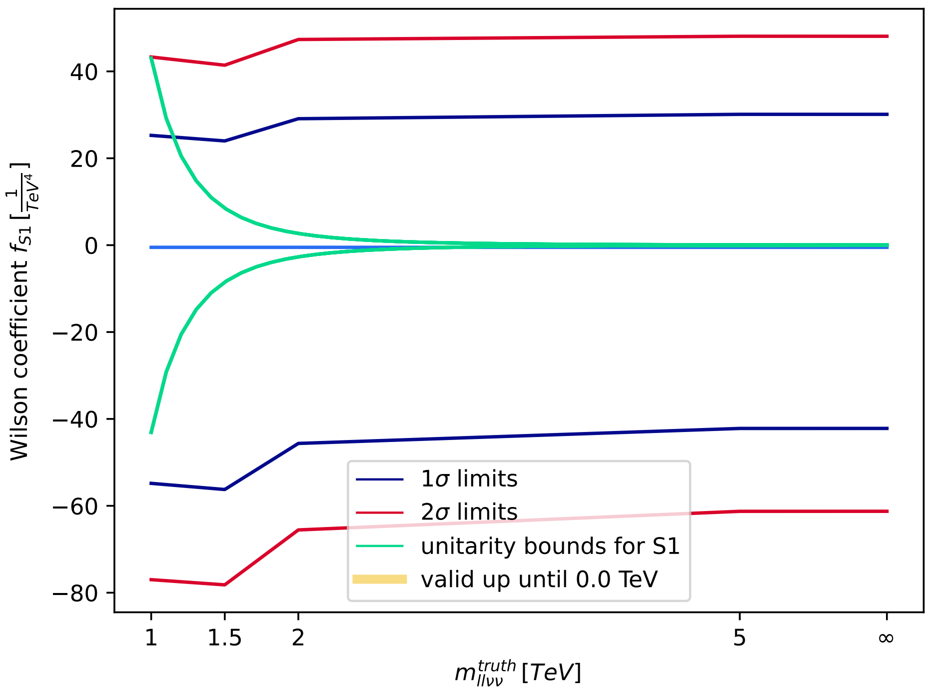

(b) WZ in CR for operator S1

Figure 8.7: Clippping scans for the EFT operator S1, for WZ in the ssWW SR (a) and the WZ control region (b).

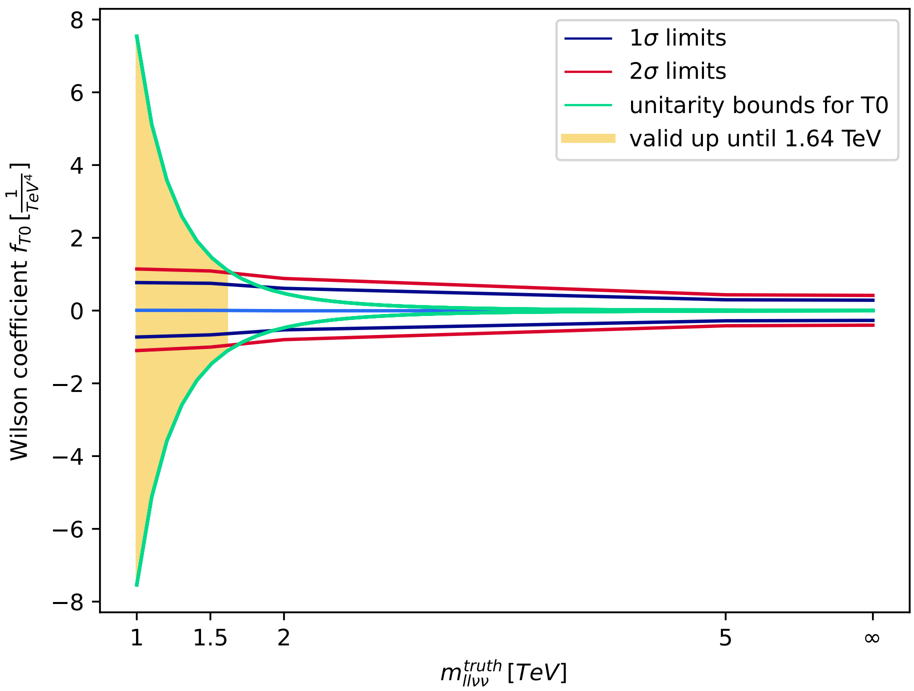

(a) ssWW in SR for operator T0

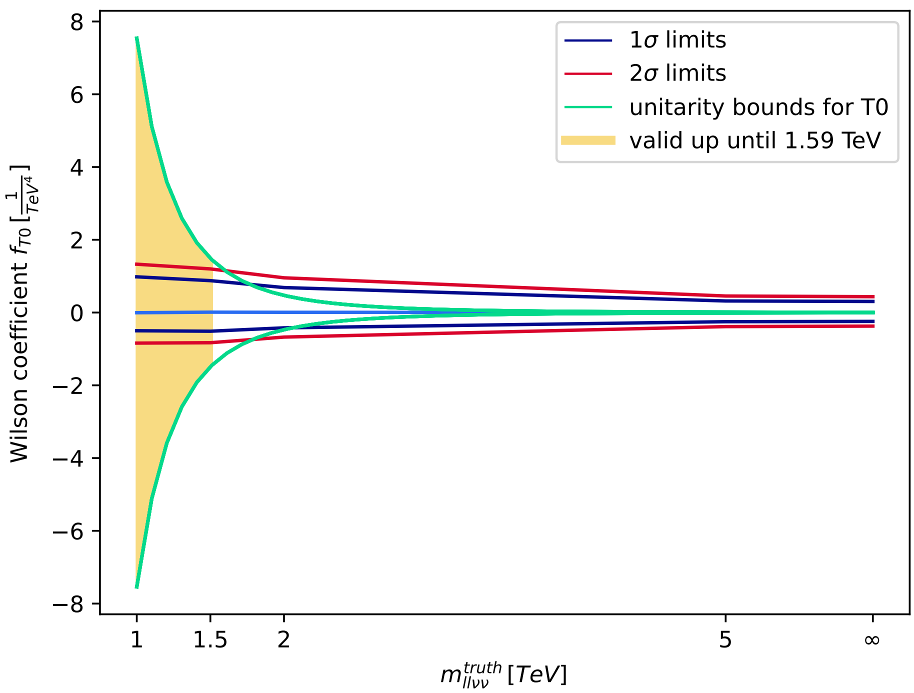

(b) combi ssWW+WZ in SR for operator T0

Figure 8.8: Clippping scans for the EFT operator T0, for ssWW (a), ssWW and WZ combined (b) in the SR.

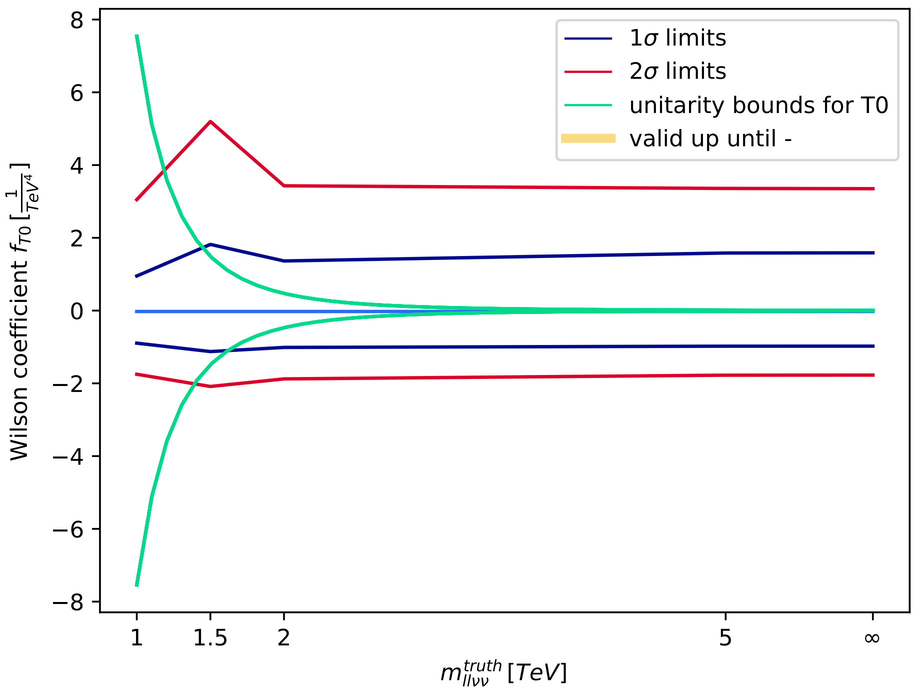

(a) WZ in SR for operator T0

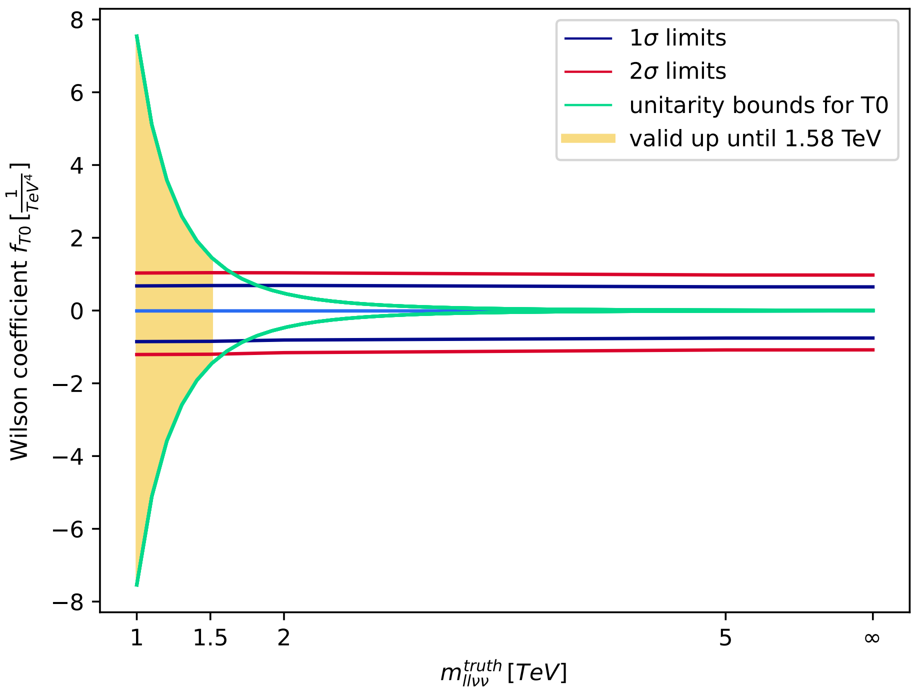

(b) WZ in CR for operator T0

Figure 8.9: Clippping scans for the EFT operator T0, for WZ in the ssWW SR (a) and the WZ control region (b).

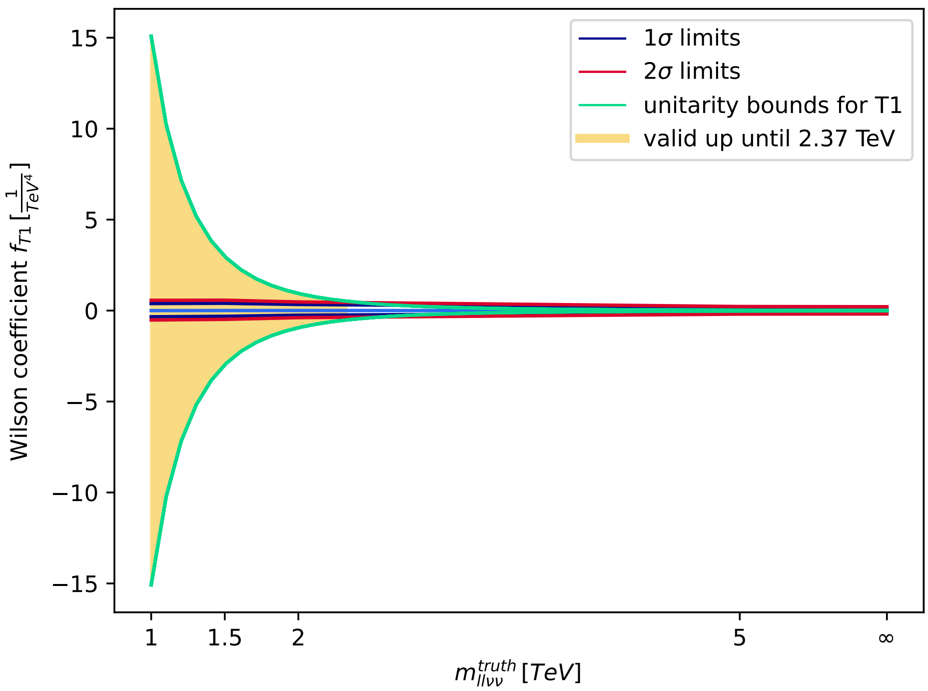

(a) ssWW in SR for operator T1

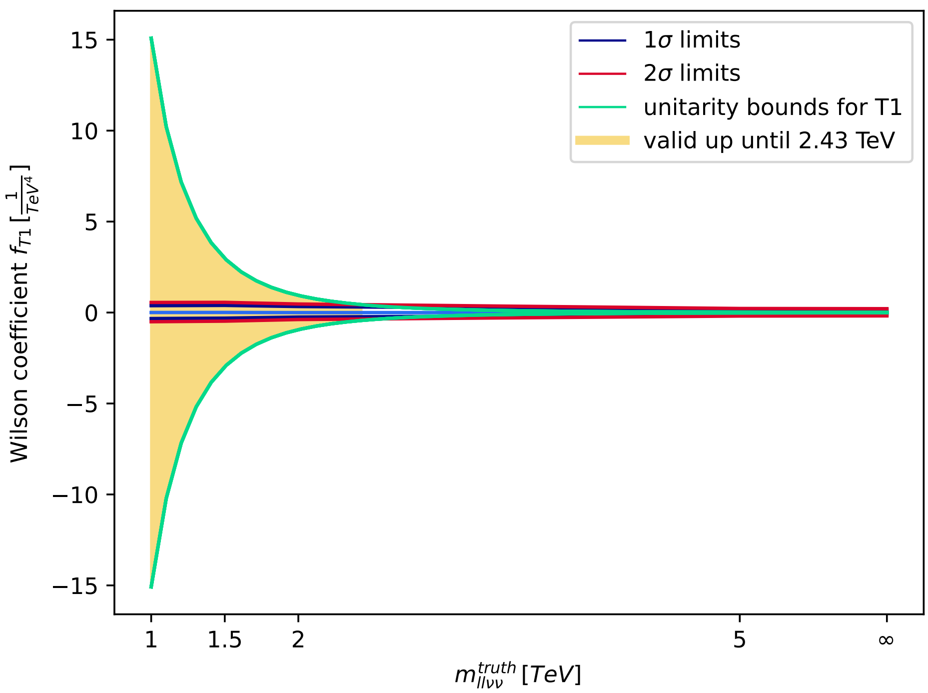

(b) combi ssWW+WZ in SR for operator T1

Figure 8.10: Clippping scans for the EFT operator T1, for ssWW (a), ssWW and WZ combined (b) in the SR.

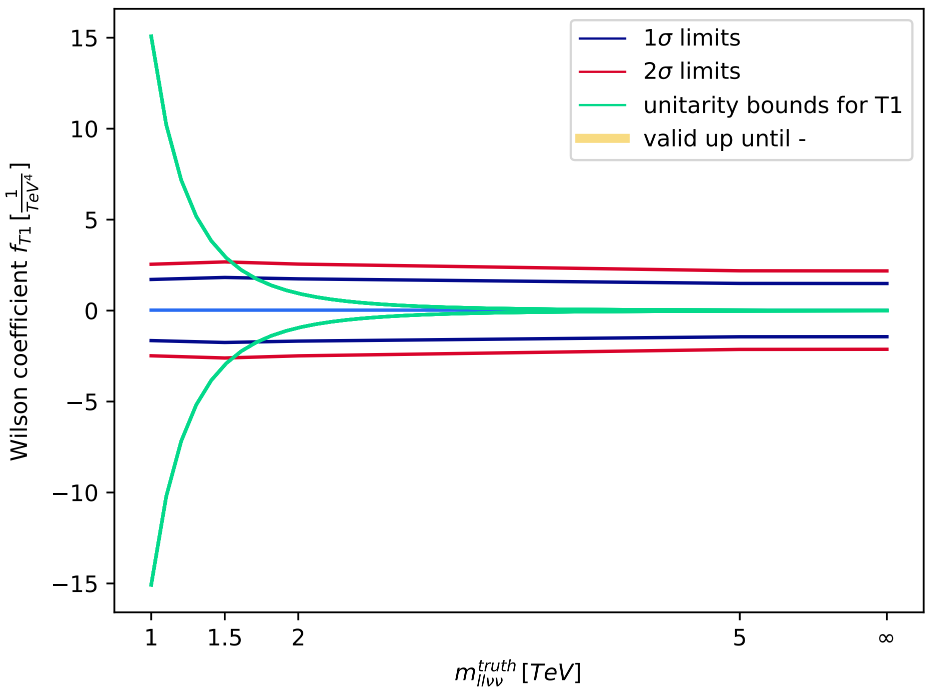

(a) WZ in SR for operator T1

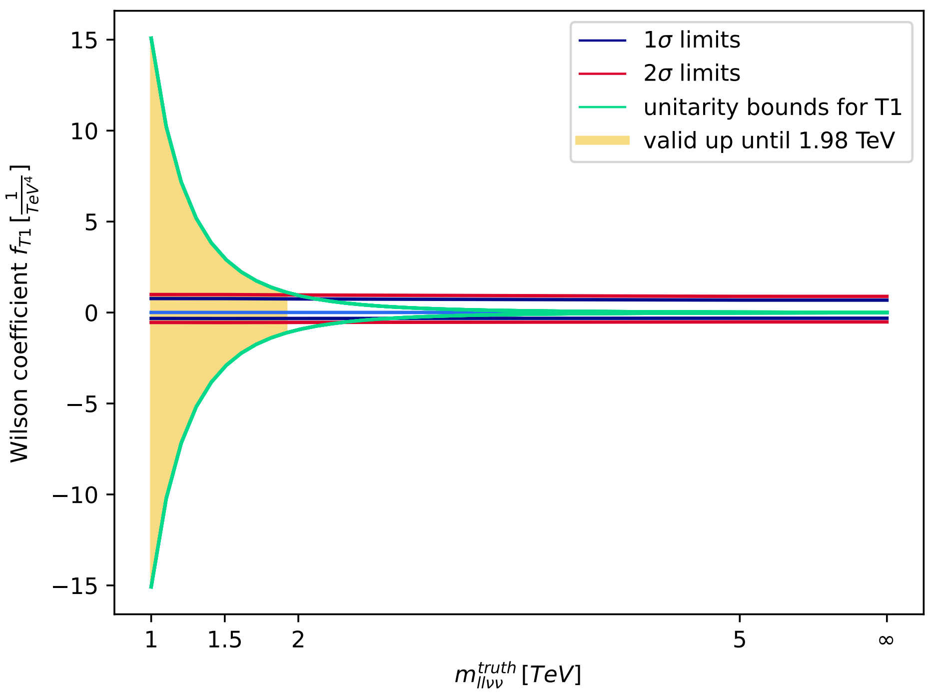

(b) WZ in CR for operator T1

Figure 8.11: Clippping scans for the EFT operator T1, for WZ in the ssWW SR (a) and the WZ control region (b).

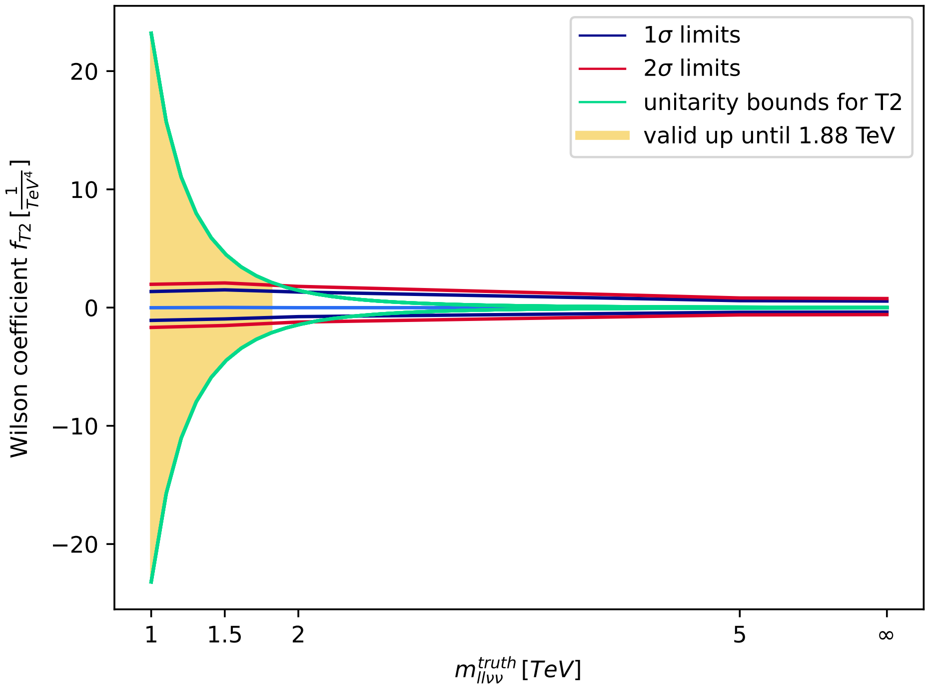

(a) ssWW in SR for operator T2

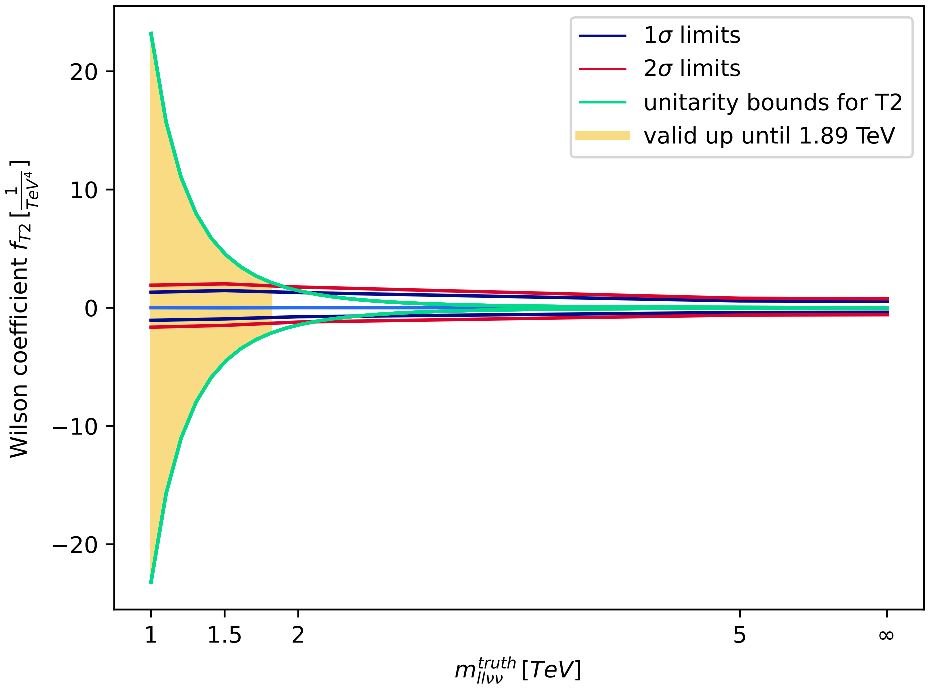

(b) combi ssWW+WZ in SR for operator T2

Figure 8.12: Clippping scans for the EFT operator T2, for ssWW (a), ssWW and WZ combined (b) in the SR.

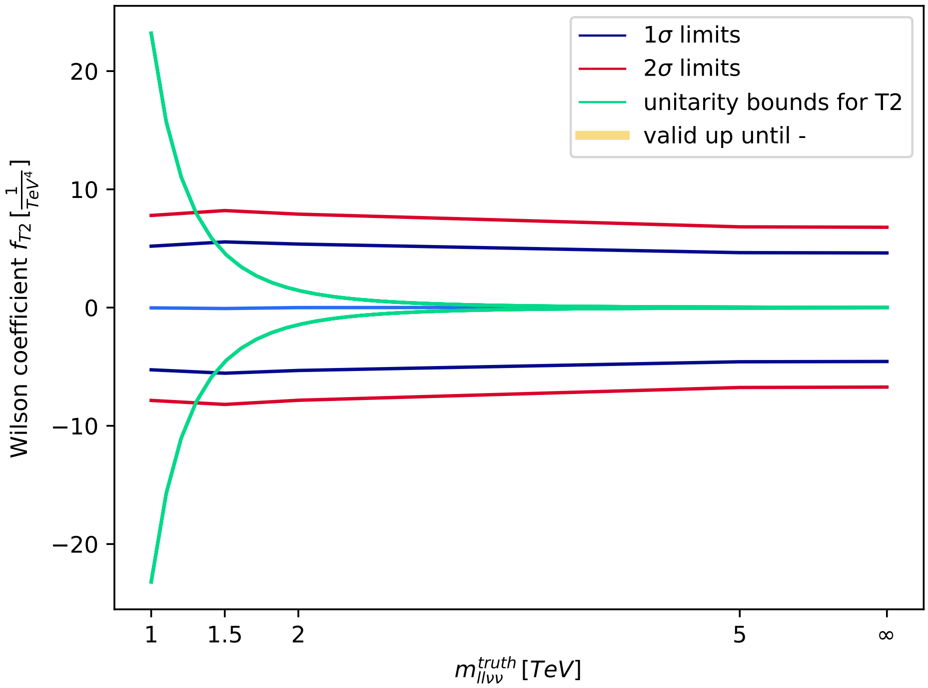

(a) WZ in SR for operator T2

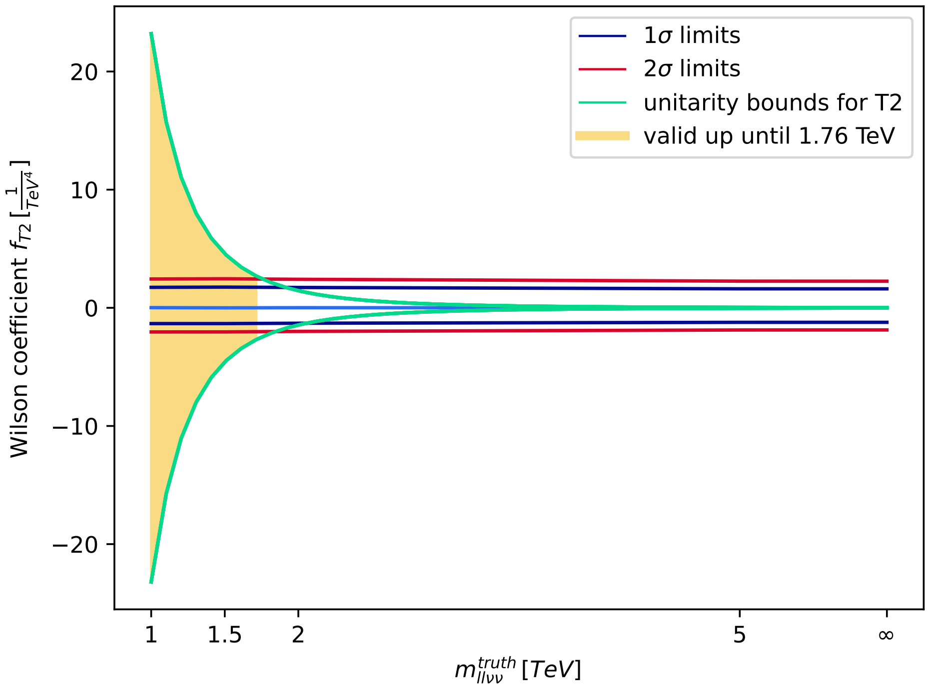

(b) WZ in CR for operator T2

Figure 8.13: Clippping scans for the EFT operator T2, for WZ in the ssWW SR (a) and the WZ control region (b).

Table 8.10: ± 1 and $\pm 2\,\sigma$ limits for ssWW (left) and combi (ssWW and WZ, on the right) in the SR for operator M0.

E_c [TeV]	best fit value	$\pm 1\sigma$		$\pm 2\sigma$		best fit value	$\pm 1\sigma$		$\pm 2\sigma$	
1	-0.029	-10.142	9.624	-15.037	14.451	-0.01	-8.531	9.915	-13.06	14.419
1.5	0.059	-8.116	7.603	-11.833	11.288	0.066	-6.719	8.188	-10.213	11.806
2	0.002	-5.863	5.575	-8.561	8.262	0.037	-4.965	6.041	-7.554	8.719
5	0.009	-3.132	3.044	-4.597	4.508	0.024	-2.956	3.125	-4.401	4.584
∞	0.012	-3.069	2.986	-4.506	4.421	0.018	-2.902	3.064	-4.32	4.495

Table 8.11: ± 1 and $\pm 2\,\sigma$ limits for ssWW (left) and combi (ssWW and WZ, on the right) in the SR for operator M1.

E_c [TeV]	best fit value	$\pm 1\sigma$		$\pm 2\sigma$		best fit value	$\pm 1\sigma$		$\pm 2\sigma$	
1	0.147	-14.811	15.995	-22.306	23.612	0.177	-14.457	14.141	-21.622	21.154
1.5	0.051	-11.713	13.66	-17.58	19.616	-0.127	-10.404	13.854	-16.128	19.433
2	0.095	-8.525	9.982	-12.803	14.307	-0.119	-7.674	10.413	-11.885	14.546
5	-0.029	-4.588	5.105	-6.868	7.395	0.066	-4.335	5.3	-6.599	7.551
∞	-0.045	-4.497	4.991	-6.729	7.233	0.038	-4.254	5.18	-6.471	7.387

Table 8.12: ± 1 and $\pm 2\,\sigma$ limits for ssWW (left) and combi (ssWW and WZ, on the right) in the SR for operator S1.

E_c [TeV]	best fit value	$\pm 1\sigma$		$\pm 2\sigma$		best fit value	$\pm 1\sigma$		$\pm 2\sigma$	
1	-0.684	-65.549	69.849	-97.23	102.26	-0.256	-40.915	88.049	-69.459	115.912
1.5	-0.246	-40.569	44.246	-59.922	63.786	-0.552	-31.874	51.097	-50.488	69.331
2	-0.1	-27.416	29.342	-40.595	42.605	-0.119	-24.208	31.721	-37.105	44.55
5	-0.114	-15.998	16.745	-23.73	24.494	-0.087	-14.919	17.645	-22.575	25.301
∞	-0.12	-15.872	16.608	-23.542	24.295	-0.116	-14.811	17.495	-22.406	25.092

Table 8.13: ± 1 and $\pm 2\,\sigma$ limits for ssWW (left) and combi (ssWW and WZ, on the right) in the SR for operator T0.

E_c [TeV]	best fit value	$\pm 1\sigma$		$\pm 2\sigma$		best fit value	$\pm 1\sigma$		$\pm 2\sigma$	
1	0.007	-0.727	0.77	-1.099	1.143	-0.005	-0.501	0.981	-0.84	1.329
1.5	0.006	-0.667	0.75	-1.004	1.089	0.01	-0.513	0.877	-0.83	1.199
2	-0.006	-0.529	0.611	-0.798	0.882	0.007	-0.421	0.686	-0.675	0.954
5	0.003	-0.28	0.297	-0.417	0.434	0.	-0.252	0.318	-0.387	0.454
∞	0.002	-0.27	0.285	-0.401	0.417	-0.003	-0.244	0.305	-0.373	0.436

Table 8.14: ±1 and ±2 σ limits for ssWW (left) and combi (ssWW and WZ, on the right) in the SR for operator T1.

E_c [TeV]	best fit value	$\pm1\sigma$		$\pm2\sigma$		best fit value	$\pm1\sigma$		$\pm2\sigma$	
1	-0.001	-0.339	0.385	-0.518	0.566	0.001	-0.33	0.378	-0.506	0.555
1.5	0.004	-0.315	0.4	-0.484	0.571	0.005	-0.308	0.393	-0.474	0.561
2	0.004	-0.253	0.335	-0.39	0.475	-0.004	-0.249	0.331	-0.384	0.469
5	-0.001	-0.127	0.157	-0.194	0.224	-0.001	-0.126	0.156	-0.193	0.223
∞	0.001	-0.122	0.148	-0.185	0.212	0.002	-0.121	0.148	-0.184	0.211

Table 8.15: ±1 and ±2 σ limits for ssWW (left) and combi (ssWW and WZ, on the right) in the SR for operator T2.

E_c [TeV]	best fit value	$\pm1\sigma$		$\pm2\sigma$		best fit value	$\pm1\sigma$		$\pm2\sigma$	
1	-0.013	-1.084	1.357	-1.679	1.969	0.008	-1.06	1.315	-1.64	1.911
1.5	0.012	-0.96	1.5	-1.517	2.082	-0.006	-0.943	1.457	-1.488	2.026
2	-0.009	-0.767	1.316	-1.224	1.793	0.011	-0.756	1.287	-1.206	1.756
5	-0.005	-0.396	0.585	-0.619	0.812	-0.006	-0.394	0.582	-0.616	0.808
∞	-0.005	-0.379	0.548	-0.591	0.763	-0.006	-0.377	0.545	-0.588	0.759

Table 8.16: ±1 and ±2 σ limits for ssWW in the SR for operator M7.

E_c [TeV]	best fit value	$\pm1\sigma$		$\pm2\sigma$	
1	0.054	-21.88	22.585	-32.94	33.466
1.5	-0.04	-18.156	18.309	-26.836	26.828
2	0.081	-13.649	12.775	-19.89	18.947
5	-0.018	-7.228	6.86	-10.566	10.189
∞	-0.005	-7.07	6.719	-10.339	9.978

Table 8.17: ±1 and ±2 σ limits for ssWW in the SR for operator S0.

E_c [TeV]	best fit value	$\pm1\sigma$		$\pm2\sigma$	
1	-0.089	-16.367	17.857	-24.347	26.085
1.5	-0.121	-9.984	11.066	-14.78	15.928
2	-0.092	-6.768	7.345	-10.041	10.644
5	0.006	-4.008	4.22	-5.95	6.167
∞	0.003	-3.974	4.182	-5.899	6.112

Table 8.18: ±1 and ±2 σ limits for WZ in the SR (left) and in the CR (right) for operator M0.

E_c [TeV]	best fit value (SR)	$\pm1\sigma$ (SR)		$\pm2\sigma$ (SR)		best fit value (CR)	$\pm1\sigma$ (CR)		$\pm2\sigma$ (CR)	
1	-0.252	-19.095	32.038	-31.068	44.326	-0.03	-1.835	1.731	-3.674	3.27
1.5	0.179	-15.172	24.716	-26.09	40.253	-0.03	-1.715	1.599	-3.448	3.002
2	-0.18	-12.417	17.944	-22.1	33.379	-0.03	-1.709	1.605	-3.427	3.026
5	-0.177	-12.932	17.566	-22.325	29.922	-0.03	-1.715	1.634	-3.424	3.11
∞	-0.177	-12.93	17.563	-22.32	29.912	-0.03	-1.715	1.634	-3.424	3.111

Table 8.19: ± 1 and $\pm 2\,\sigma$ limits for WZ in the SR (left) and in the CR (right) for operator M1.

E_c [TeV]	best fit value (SR)	$\pm 1\sigma$ (SR)		$\pm 2\sigma$ (SR)		best fit value (CR)	$\pm 1\sigma$ (CR)		$\pm 2\sigma$ (CR)	
1	-0.426	-38.495	32.839	-59.759	52.332	-0.151	-14.742	9.214	-20.26	14.61
1.5	-0.477	-26.776	43.851	-46.092	65.954	-0.151	-14.394	8.871	-19.94	14.162
2	-0.367	-24.056	43.983	-41.849	65.628	-0.151	-14.191	8.601	-19.563	13.748
5	-0.231	-22.907	41.09	-39.142	59.474	-0.151	-14.212	7.873	-19.296	12.741
∞	-0.232	-22.901	41.079	-39.129	59.451	-0.151	-14.203	7.87	-19.283	12.736

Table 8.20: ± 1 and $\pm 2\,\sigma$ limits for WZ in the SR (left) and in the CR (right) for operator S1, note the double minimum described in subsection 4.2.

E_c [TeV]	best fit value (SR)	$\pm 1\sigma$ (SR)		$\pm 2\sigma$ (SR)		best fit value (CR)	$\pm 1\sigma$ (CR)		$\pm 2\sigma$ (CR)	
1	-0.754	-60.18	68.447	-116.417	363.512	-0.503	-54.83	25.267	-76.998	43.312
1.5	-0.754	-69.078	241.899	-127.004	321.965	-0.503	-56.246	23.991	-78.19	41.422
2	-0.754	-80.16	199.66	-138.342	261.414	-0.503	-45.641	29.105	-65.548	47.342
5	-0.754	-77.757	181.471	-132.533	238.443	-0.503	-42.19	30.114	-61.267	48.089
∞	-0.754	-77.751	181.444	-132.521	238.408	-0.503	-42.185	30.111	-61.259	48.084

Table 8.21: ± 1 and $\pm 2\,\sigma$ limits for WZ in the SR (left) and in the CR (right) for operator T0; note that due to software insufficiency and double minima those values are to be treated with caution, for more information see subsection 4.2.

E_c [TeV]	best fit value (SR)	$\pm 1\sigma$ (SR)		$\pm 2\sigma$ (SR)		best fit value (CR)	$\pm 1\sigma$ (CR)		$\pm 2\sigma$ (CR)	
1	-0.025	-0.895	0.951	-1.75	3.049	-0.01	-0.854	0.677	-1.21	1.031
1.5	-0.025	-1.127	1.819	-2.086	5.197	-0.01	-0.847	0.686	-1.201	1.04
2	-0.025	-1.013	1.364	-1.878	3.43	-0.01	-0.81	0.69	-1.158	1.037
5	-0.025	-0.979	1.582	-1.776	3.357	-0.01	-0.757	0.651	-1.083	0.977
∞	-0.025	-0.978	1.587	-1.773	3.35	-0.01	-0.755	0.65	-1.081	0.975

Table 8.22: ± 1 and $\pm 2\,\sigma$ limits for WZ in the SR (left) and in the CR (right) for operator T1.

E_c [TeV]	best fit value (SR)	$\pm 1\sigma$ (SR)		$\pm 2\sigma$ (SR)		best fit value (CR)	$\pm 1\sigma$ (CR)		$\pm 2\sigma$ (CR)	
1	0.025	-1.649	1.711	-2.485	2.547	0.005	-0.325	0.769	-0.545	0.989
1.5	0.025	-1.753	1.821	-2.606	2.676	0.005	-0.33	0.767	-0.55	0.988
2	0.025	-1.678	1.744	-2.489	2.556	0.005	-0.326	0.748	-0.542	0.965
5	0.025	-1.441	1.493	-2.135	2.187	0.005	-0.312	0.684	-0.516	0.888
∞	0.025	-1.436	1.488	-2.128	2.181	0.005	-0.312	0.683	-0.515	0.886

Table 8.23: ± 1 and $\pm 2\,\sigma$ limits for WZ in the SR (left) and in the CR (right) for operator T2.

E_c [TeV]	best fit value (SR)	$\pm 1\sigma$ (SR)		$\pm 2\sigma$ (SR)		best fit value (CR)	$\pm 1\sigma$ (CR)		$\pm 2\sigma$ (CR)	
1	-0.025	-5.262	5.193	-7.853	7.792	0.015	-1.336	1.732	-2.042	2.439
1.5	-0.078	-5.551	5.554	-8.191	8.205	-0.002	-1.334	1.751	-2.039	2.458
2	-0.001	-5.319	5.371	-7.839	7.903	0.01	-1.305	1.722	-1.995	2.414
5	0.025	-4.583	4.646	-6.758	6.828	-0.007	-1.229	1.609	-1.876	2.258
∞	0.024	-4.559	4.621	-6.723	6.792	-0.008	-1.227	1.606	-1.873	2.253